ARTICLE

Disrupted Development of the mPFC-Thalamic Circuit in Shank3$^{-/-}$ mice, an autism-associated model

Gabrielle Devienne[1], Gil Vantomme[1] and John R. Huguenard[1]✉

© The Author(s), under exclusive licence to Springer Nature Limited 2025

Autism Spectrum Disorders (ASDs) are a group of neurodevelopmental disorders with heterogeneous causes, and are characterized by communication deficits, impaired social interactions, and repetitive behaviors. Despite numerous studies in mouse models focused on pathophysiological circuit mechanisms of ASD in mature animals, little is known regarding ASD onset and its evolution through development. The medial prefrontal cortex (mPFC) is crucial for higher-order cognitive functions and social behavior, thus key to understanding ASD pathology. To explore early developmental disruptions in the mPFC, we used the *Shank3* knockout (Shank3$^{-/-}$) mouse model. SHANK3 is crucial for glutamatergic synapse maturation, and the Shank3$^{-/-}$ mouse has been well-characterized for displaying ASD-related behavioral phenotypes. We investigated network, cellular, and synaptic changes within the mPFC and in its projections to the mediodorsal thalamus (MD) at two developmental stages, preweaning (P14) and adulthood (>P55). Our findings reveal early synaptic deficits at P14 both within the mPFC and in its projections to the MD accompanied by alterations in mPFC network activity and reduced excitability of excitatory neurons, overall suggesting hypofunction. Interestingly, behavioral deficits were already detectable by P11, preceding the observation of synaptic changes at P14. By adulthood, these early synaptic and cellular alterations progressed to global dysfunction, characterized by mPFC network hyperfunction and layer 5 pyramidal cell hyperexcitability, accompanied by augmented glutamatergic signaling to MD with enhanced action potential production. These results suggest that early synaptic changes may precede and interact with behavioral deficits, which might lead to compensatory mechanisms that contribute to more pronounced mPFC dysfunction later in development. This study highlights the complex dynamic progression of mPFC deficits in ASD and emphasizes the relevance of early synaptic alterations as potential contributors to later behavioral and cognitive deficits.

Molecular Psychiatry; https://doi.org/10.1038/s41380-025-03390-6

INTRODUCTION

Autism Spectrum Disorders (ASDs) refer to a group of neurodevelopmental disorders characterized by communication deficits, impaired social interaction, and repetitive behaviors. ASD arises from complex etiologies including genetic causes and prenatal insults, making it difficult to precisely determine its onset across individuals. In humans, the behavioral deficits related to ASD are generally first observed around the second year of life [1, 2], a period associated with rapid maturation of the medial prefrontal cortex (mPFC) [3]. Abnormal mPFC development is hypothesized to contribute to ASD symptoms [4–6], given its critical role in regulating social behavior [5, 7–9]. In mouse, communication deficits can be perceived in the early postnatal periods (pre-weaning; <P21) [10, 11] a critical window for morphological and functional mPFC development [12]. It is around the same period that mPFC develops long range connections with subcortical areas [12, 13] including reciprocal connections with the mediodorsal thalamus (MD) [14].

SHANK3, a scaffolding protein critical for glutamatergic synapse maturation [15], is the product of a gene strongly associated with ASD [16, 17]. The Shank3$^{-/-}$ mouse model [11] recapitulates many ASD-related phenotypes, including social deficits and communication impairments. While most *Shank3* mutations in humans are heterozygous, the full knockout provides a clearer framework for dissecting synaptic mechanisms by amplifying phenotypic effects, thereby facilitating the identification of cellular and circuit-level alterations [18]. Interestingly, SHANK3 protein levels naturally decline around P14 during normal development [19], coinciding with a reduction in connectivity between the mPFC and the MD [20]. This developmental window offers a unique opportunity to investigate how early synaptic changes might predispose the mPFC-MD circuit to later dysfunction. By studying the Shank3$^{-/-}$ model at both P14 and adulthood (>P55), we aim to determine whether early synaptic alterations are present and whether they evolve into later deficits in network and behavioral function.

To investigate mPFC disruptions in Shank3$^{-/-}$ mice, we compared network, cellular, and synaptic properties at P14 and adulthood (>P55). Behavioral assessments confirmed communication deficits as early as P11 [11] as well as social deficits in adulthood [11, 21], emphasizing the early onset and persistence of ASD-related symptoms. Electrophysiological methods, including local field potential (LFP) and whole-cell patch-clamp recordings, were used to examine mPFC activity. We also tested mPFC-MD circuit function using optogenetic stimulation of mPFC axons and intracellular recordings in MD cells.

Our findings reveal a dynamic progression of mPFC deficits in Shank3$^{-/-}$ mice. At P14, mPFC hypoexcitability was observed in

[1]Department of Neurology and Neurological Sciences, Stanford University, Stanford, CA, USA. ✉email: huguenard@stanford.edu

Received: 29 January 2025 Revised: 15 October 2025 Accepted: 2 December 2025
Published online: 16 December 2025

upper layer pyramidal cells, with synaptic excitatory-inhibitory imbalance in layer 5. Despite an overall mPFC network hypoexcitability, optogenetic stimulation of mPFC-MD projections revealed exuberant and long-lasting synaptic excitation in MD cells, an early sign of circuit hyperexcitability. In adulthood, pronounced mPFC network hyperactivity emerged, particularly in layer 5 pyramidal cells that project to the MD. Long lasting excitatory synaptic responses in MD cells were persistently augmented in Shank3$^{-/-}$ mice, indicating long-term disruptions in mPFC-MD connectivity.

These results show that early synaptic changes in Shank3$^{-/-}$ mice precede pronounced network dysfunction in adulthood. Mixed findings at P14 suggest compensatory mechanisms may temporarily mask mPFC dysfunction, highlighting critical periods of vulnerability in ASD and the potential for early interventions to mitigate long-term deficits.

RESULTS

Early emergence of social behavioral deficits in Shank3$^{-/-}$ mice

To assess the development of potential SHANK3-related behavioral deficits, we tested WT and Shank3$^{-/-}$ mice at two distinct developmental stages: pups (P11) and adults (>P55). Given the limited mobility of pre-weaning pups, ultrasonic vocalizations (USV) were used as a proxy of social behavior [22]. Upon social isolation Shank3$^{-/-}$ P11 pups produced many fewer calls compared to their wild type (WT) littermates (Fig. 1A-D; mean ± sem; WT: 132.5 ± 34.2 calls; Shank3$^{-/-}$: 16 ± 7.4 calls; testing period 8 minutes; Mann-Whitney, $p = 0.02$). Additionally, we analyzed the distribution of USV categories (Fig S1) and observed significant differences between genotypes. A chi-square test comparing WT and Shank3$^{-/-}$ mice revealed a highly significant shift in call type ratios (χ^2, $p < 0.0001$). Specifically, *harmonic* (Category #8) and *short ascent* (Category #11) calls were markedly underrepresented in Shank3$^{-/-}$ mice—occurring approximately 5 times less than expected based on standard residual analysis ($p < 0.01$). Interestingly, as the overall call distribution shifted, WT mice showed a higher proportion of harmonic calls. The *multisyllabic* category (Category #9) was also reduced in Shank3$^{-/-}$ mice (1.5 times less than expected, $p < 0.05$). Conversely, *complex* (Category #10) and *arc down* (Category #5) calls were 1.5 times more frequent than expected in Shank3$^{-/-}$ mice ($p < 0.05$), suggesting a qualitative alteration in the USVs repertoire.

Consistent with social deficits persisting into adulthood, mature Shank3$^{-/-}$ mice failed to show a social preference in a social interaction test, showing similar times with either a novel inanimate object or a novel conspecific mouse. In contrast, adult WT mice showed a strong social preference (Fig. 1 E-G; interaction time, mean ± sem; WT: mouse, 33.1 ± 4.95, object, 15.8 ± 1.95%, paired t-test, $p = 0.02$; Shank3$^{-/-}$: mouse, 14.6 ± 5.62, object: 15.8 ± 5.91%, paired t-test, $p = 0.89$). These results align with previous literature on ASD mouse models [23–25], including the complete Shank3 knockout used here [11]. We therefore confirm that behavioral deficits in this model begin as early as P11, which correlates with a period of critical development of the corticothalamic network connecting the mPFC to the MD [12, 14], an important circuit related to social behavior [26].

Developmental progression of hyperexcitability in the mPFC network

To investigate potential SHANK3-related disruptions in mPFC development, we first employed an in vitro extracellular recording approach to evaluate network excitability. We obtained coronal brain slices containing the mPFC from Shank3$^{-/-}$ mice and WT littermates at different developmental stages, including P11, P14, and adulthood (Fig. 2 and Figure S2). Using a 16-shank linear silicon probe array positioned normal to the pial surface of mPFC, we recorded network activity in the form of local-field potentials (LFPs). Local electrical stimulation of deep layers evoked multi-component LFPs that could be observed across all cortical layers, demonstrating engagement of intra-cortical circuits (Fig. 2A). To localize the LFP signals to different cortical layers, we calculated the current source density [27] (CSD) as the second spatial derivative of the LFP (Fig. 2B and C). This allowed us to compare mPFC network differences between Shank3$^{-/-}$ mice and WT littermates. We observed matched pairs of sinks and sources in the CSD profiles following local electrical stimulation in the deep layers. Sinks are negative CSD signals generally attributed to the movement of cations from the extracellular space into the cells during synaptic excitation. Given conservation of charge, such ionic current flow must be matched with a paired outward flow of cations (sources) from these cells at a distance from the original sinks. Synaptic inhibition has the opposite sinks/source polarity as it is mainly associated with anionic, rather than cationic, current flow. Accordingly, sources/sinks cannot unambiguously be associated with either excitation or inhibition. However given that the majority of synapses in neocortical circuits are excitatory [28–30], sinks will generally be dominated by excitatory synaptic signals, and sources with their return path. We applied a subtractive pharmacological approach to isolate components of the CSD signal, to reveal distinct pre- and post-synaptic components, with the post-synaptic components essentially blocked by DNQX and CPPene, AMPA and NMDA receptor antagonists (Figure S1A2, B), and presynaptic components blocked by TTX.

We initially assessed mPFC excitability at the two stages that we had previously characterized behaviorally, P11 and adult. At P11 we observed LFP and CSD components generally comparable to what was observed in adult mice, although with somewhat simpler features especially noted as more monophasic responses, consistent with the immature state of the network at P11 (Fig. 2A, vs. Figure S2C). We did not detect any differences between Shank3$^{-/-}$ mice and their WT littermates at this stage. We then selected P14 as the next developmental time point. This is a developmental stage marked by significant changes in SHANK3 protein levels [19]. The CSD signal at P14 showed sinks and sources across layers that were more complex (multiphasic) than at P11, and more similar to the CSD responses in adults. At P14, both the previously identified postsynaptic sinks and sources (Figure S2B) were similar between Shank3$^{-/-}$ mice and WT littermates. However, we observed a significant reduction of the presynaptic source located in layer 5 (Fig. 2C, component 3), with little to no reduction in presynaptic sink in layer 2/3 (component 1) in Shank3$^{-/-}$ mice compared to WT littermates (Figure 2CD P14; two-way ANOVA with repeated measures: genotype $p = 0.03$, stimulation $p < 0.0001$, interaction $p < 0.0001$ for the layer 5 presynaptic source). This reduction in CSD signal may reflect a hypofunction of mPFC at this stage of development, in particular of the presynaptic recruitment of the cortical network. By contrast, at adulthood, mPFC slices from Shank3$^{-/-}$ mice showed an overall *increase* in sinks and sources across layers (components 1–4, Fig. 2B-D). Closer inspection revealed that this overall increase in CSD signal in adult is mediated by an increase in the peak amplitude of the layer 2/3 presynaptic sink and the layer 5 presynaptic source and postsynaptic sink (Fig. 2CD Adults; 2-way ANOVA with repeated measure, layer 2/3 presynaptic sink: genotype $p = 0.004$, stimulation $p < 0.0001$, interaction $p < 0.0001$; layer 5 presynaptic source: genotype $p = 0.001$, stimulation $p < 0.0001$, interaction $p < 0.0001$, layer 5 postsynaptic sink: genotype $p = 0.01$, stimulation $p < 0.0001$, interaction $p = 0.04$). There is also a trend for an increase in the peak amplitude of layer 2/3 postsynaptic source in adult Shank3$^{-/-}$ mice (Fig. 2D Adults; 2-way ANOVA with repeated measure, layer 2/3 postsynaptic source: genotype $p = 0.051$, stimulation $p < 0.0001$, interaction $p = 0.08$). Altogether, these data demonstrate the emergence of a hyperfunctional mPFC network between P14 and adulthood (>P55) in the Shank3$^{-/-}$ mouse model, characterized by early-stage hypoexcitability at P14 followed by hyperexcitability in adulthood, reflecting a developmental shift in network dynamics.

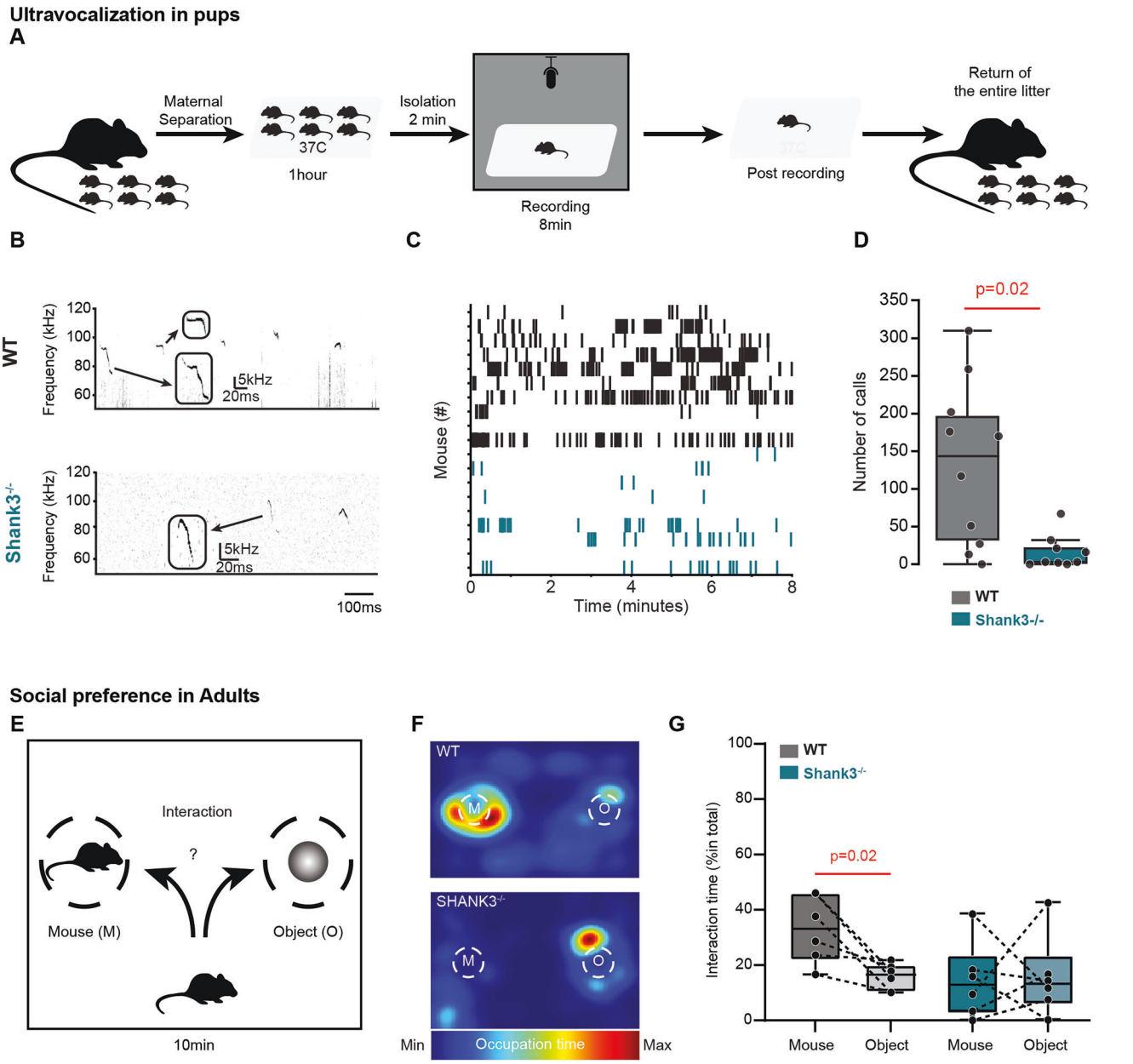


Fig. 1 Shank3$^{-/-}$ mice display deficits in communication in early life and in social behavior in adulthood. A Schematic diagram of isolation and ultrasonic vocalization protocol performed in Shank3 WT and Shank3$^{-/-}$ P11 littermates. **B** Examples of 1 second long spectra (bottom images) from USV recordings in WT and Shank3$^{-/-}$ mice. Insets show examples of individual syllables expanded as indicated by arrows in the original recordings. Top: WT (black); Bottom: Shank3 (blue). **C** Raster plot showing individual mouse ultrasonic vocalization (USV) calls during 8-minute recordings, with WT mice represented in black and Shank3$^{-/-}$ in blue **D** Number of calls for WT (grey) and Shank3$^{-/-}$ (blue). **E** Schematic diagram of social preference test performed in WT and Shank3$^{-/-}$ adults. **F** Example of occupation time heat maps for WT (top) and Shank3$^{-/-}$ (bottom) adults. **G** Percentage of the interaction time with a never-met conspecific (darker colors) or a novel inanimate object (lighter colors) for WT (grey) and Shank3$^{-/-}$ (blue).

Developmental emergence of hyperexcitability of layer 5 mPFC pyramidal cells

Our in vitro LFP experiments revealed increased mPFC network activity in Shank3$^{-/-}$ adult mice, evidenced in both pre- and postsynaptic signals. These results suggest potential alterations in the properties of local mPFC cells and/or in the synaptic connections within the mPFC. Excitatory pyramidal neurons in the mPFC are crucial for regulating cognitive and social behavior [31]. Layer 2/3 of the mPFC receives diverse long-range inputs, including notable projections from the MD thalamus [32]. Conversely, layer 5 of the mPFC primarily projects to the MD thalamus, although not exclusively [12, 33, 34] as it can target other subcortical areas along with the contralateral mPFC.

To investigate developmental changes in cellular excitability, we recorded mPFC layer 2/3 and layer 5 pyramidal cells at P14 and in adulthood (>P55). Consistent with decreased excitability observed in the LFP (Fig. 2D), early in development L2/3 pyramidal cells revealed hypoexcitability, in particular with a hyperpolarized resting membrane potential (Fig. 3A; RMP, P14; mean ± sem; WT: −58.6 ± 1.3 vs Shank3$^{-/-}$: −62.8 ± 1.3; p = 0.03, Welsh t-test) which is not observed in adults. In addition, we found that these cells fired significantly fewer action potentials in response to

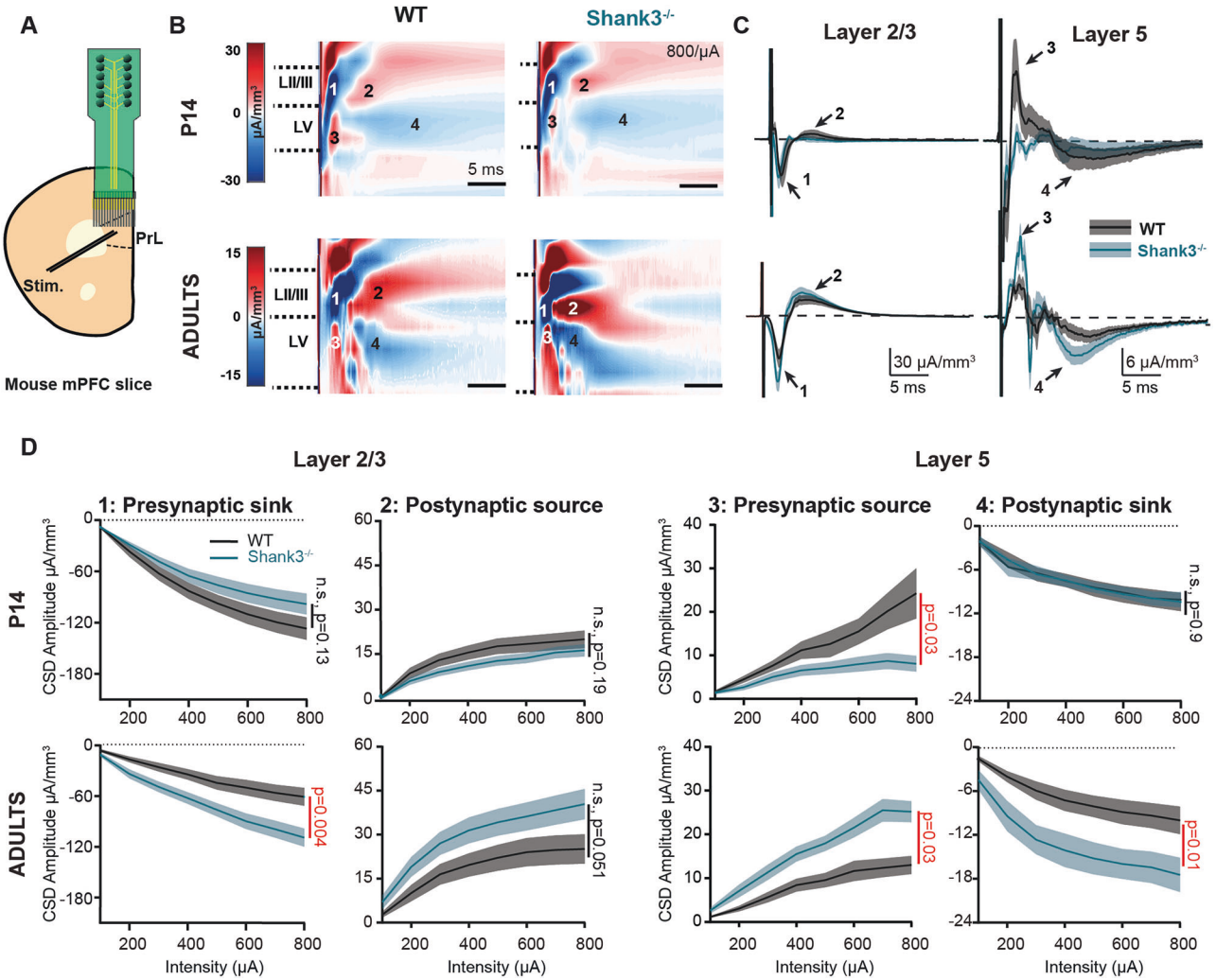


Fig. 2 Shank3$^{-/-}$ mice display mPFC hypofunction in early life and hyperfunction in adulthood. A Schematic of LFP recording across all mPFC layers in response to electrical stimulation delivered to deep layers. **B** Average current source density (CSD) response displayed as a heat map of mPFC network activity in response to a near maximal (800 µA) stimulation in WT (left) and Shank3$^{-/-}$ (right) at P14 (top row; WT = 3 mice, 10 slices; Shank3$^{-/-}$ = 3 mice, 11 slices) and adults (>P55, bottom row; WT = 5 mice, 12 slices; Shank3$^{-/-}$ = 5 mice, 13 slices). **C** Average CSD response of the L2/3 presynaptic sink (arrow 1, numbers correspond to those in B), L2/3 postsynaptic source (arrow 2), L5 presynaptic source (arrow 3) and L5 postsynaptic sink (arrow 4) in P14 (upper) and adult (lower) slices. Traces represent mean (solid line) ± SEM (shaded line). **D** Input/ Output curve of CSD peak amplitude as a function stimuli intensity for P14 (top row) and adults (bottom row); WT (grey) and Shank3$^{-/-}$ (blue).

depolarizing current steps (Fig. 3B; 2-way ANOVA; genotype $p = 0.0002$, current injection $p < 0.0001$, interaction $p < 0.0001$. Layer 2/3 was no longer hypoexcitable in adulthood (Fig. 3C).

Various ASD mouse models have been shown to display hyperexcitability of adult mPFC layer 5 pyramidal cells [5, 35, 36]. Consistent with this, we find that in Shank3$^{-/-}$ mice layer 5 pyramidal cells have a depolarized RMP (Fig. 3D; RMP; Adults; mean ± sem; WT: −67 ± 1.3 vs Shank3$^{-/-}$: −63.4 ± 1.2, $p = 0.048$, Welsh t-test). Similar results were observed at P14 (Fig. 3D; RMP; P14; mean ± sem; WT: −63 ± 1.3 vs Shank3$^{-/-}$: −57.4 ± 1.4, $p = 0.005$, Welsh t-test). This early sign of hyperexcitability is also reflected by a higher input resistance (Fig. 3D; RMP; P14; mean ± sem; WT: 304 ± 29 vs Shank3$^{-/-}$: 448 ± 33, $p = 0.003$, Welsh t-test). At P14, layer 5 pyramidal cells displayed similar action potential numbers in response to a range of depolarizing current injections in Shank3$^{-/-}$ and WT littermates (Fig. 3E). Interestingly, in Shank3$^{-/-}$ adult layer 5 pyramidal cells display higher number of action potentials (Fig. 3F; 2-way ANOVA; genotype $p < 0.0001$, current injection $p < 0.0001$, interaction $p < 0.0001$). Cells with depolarizing block were excluded from the main figure (Fig. 3C and F) but including them in the analysis (Figure S3C) did not alter the results. In addition, these cells also display an increased hyperpolarization induced membrane potential sag + rebound compared to their WT littermates (Figure S3 B, $p = 0.04$, Mann Whitney test). We did not observe any alterations in individual action potential properties at any age or in any layer (Figure S3).

Biocytin was included in our intracellular recording solution, which allowed us to recover the cellular morphology of a subset of mPFC layer 5 pyramidal cells in both WT and Shank3$^{-/-}$ at P14 and in adults. A Scholl analysis revealed an increase in dendritic complexity in Shank3$^{-/-}$ cells already at P14, which persisted into adulthood (Figure S4B; 2-way ANOVA, P14, genotype $p = <0.0001$, distance $p = <0.0001$, interaction $p = <0.0001$; Adults, genotype $p = <0.0001$, distance $p = <0.0001$, interaction $p = <0.0001$). Shank3$^{-/-}$ neurons had more arborizations near the soma and more branches overall compared to WT, while the average neurite length was similar (Figure S4C, D, E; FigS5 and 6). It has been described that layer 5 pyramidal cells can be split in at least two different subtypes: subcortically projecting, thick-tufted neurons that display a marked H-current and related hyperpolarization

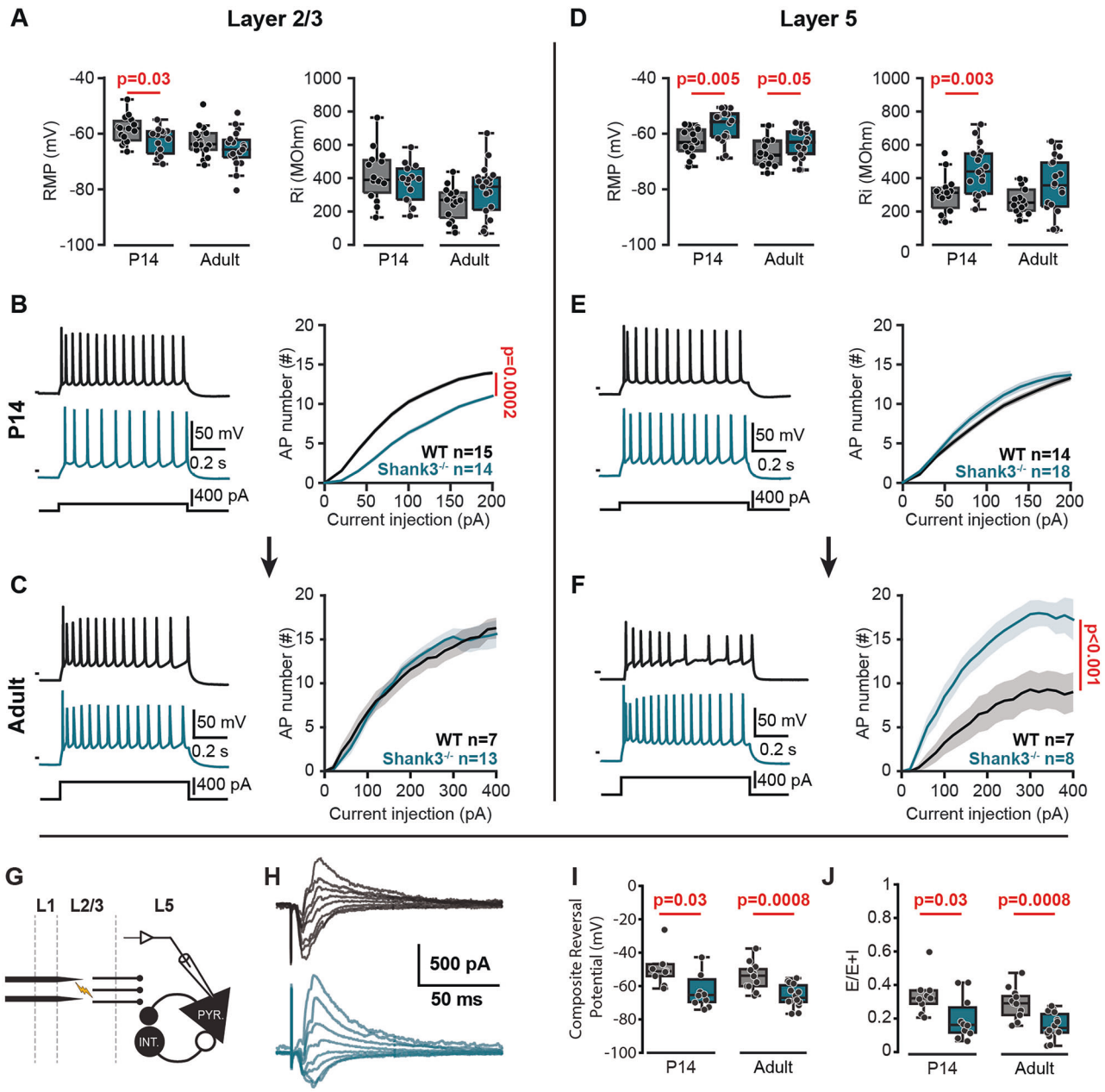


Fig. 3 Shank3$^{-/-}$ mice display early electrophysiological hypoexcitability in mPFC layer 2/3 that develops into hyperexcitability of layer 5 in adulthood. A Resting membrane potential (RMP, left) and input resistance (Ri, right) of layer 2/3 pyramidal neurons from P14 and adult WT (grey) and Shank3$^{-/-}$ (blue) mice. **B** Left, representative action potential trains in layer 2/3 mPFC pyramidal cells in response to 100 pA, 800 ms current injection at P14. Right, number of APs in layer 2/3 pyramidal cells at P14. **C** Same as (**B**), recorded in adult mice in response to 400 pA current injection for 800 ms. Traces represent mean ± sem. **D** Resting membrane potential (RMP, left) and input resistance (Ri, right) of layer 5 pyramidal neurons from P14 and adult WT (grey) and Shank3$^{-/-}$ (blue) mice. **E** Left, representative action potential responses of layer 5 mPFC pyramidal cells at P14 (100 pA stimulus). Right, number of APs in layer 5 pyramidal cells at P14. Traces represent mean ± SEM. **F** Same as (**E**), in adult mice using a 400 pA current injection. Only cells without depolarization block are included in AP number analysis. (**G–J**). Synaptic current–voltage (I/V) analysis of mPFC layer 5 pyramidal cells. **G** Schematic of experimental configuration. Electrical stimulation was delivered in layer 2/3, and postsynaptic currents were recorded in layer 5 pyramidal cells across a holding potential range from −100 to −30 mV. **H** Example current responses across this range of potentials from adult WT (grey) and Shank3$^{-/-}$ (blue) cell. **I** Composite synaptic reversal potential (Erev) measured at the time of maximal synaptic conductance for each cell. **J** Estimated excitatory/inhibitory ratio (E/(E + I)) calculated from the composite Erev, assuming inhibitory and excitatory reversal potentials of −80 mV and + 10 mV, respectively.

induced membrane potential sag (pyramidal tract (PT) cells), and callosal projecting (intratelencephalic (IT) cells), thin-tufted neurons that display a reduction in H-current [37, 38].

We measured apical dendritic shaft width in WT and Shank3$^{-/-}$, and these did not show any differences (Figure S3F) suggesting that our morphological analysis was performed in comparable mPFC neuron populations. Moreover, we examined the firing adaptation profiles of recorded cells [5] and found no evidence for the emergence of two distinct populations in either genotype (Figure S3D). Finally, while classification based on sag and rebound reliably distinguished the two subtypes in WT mice, this approach was not applicable in Shank3$^{-/-}$ mice, likely due to the known interaction between Shank3 and H-current mechanisms, which leads to increased sag + rebound value in these cells (FigS3B). To ensure that the observed effects were

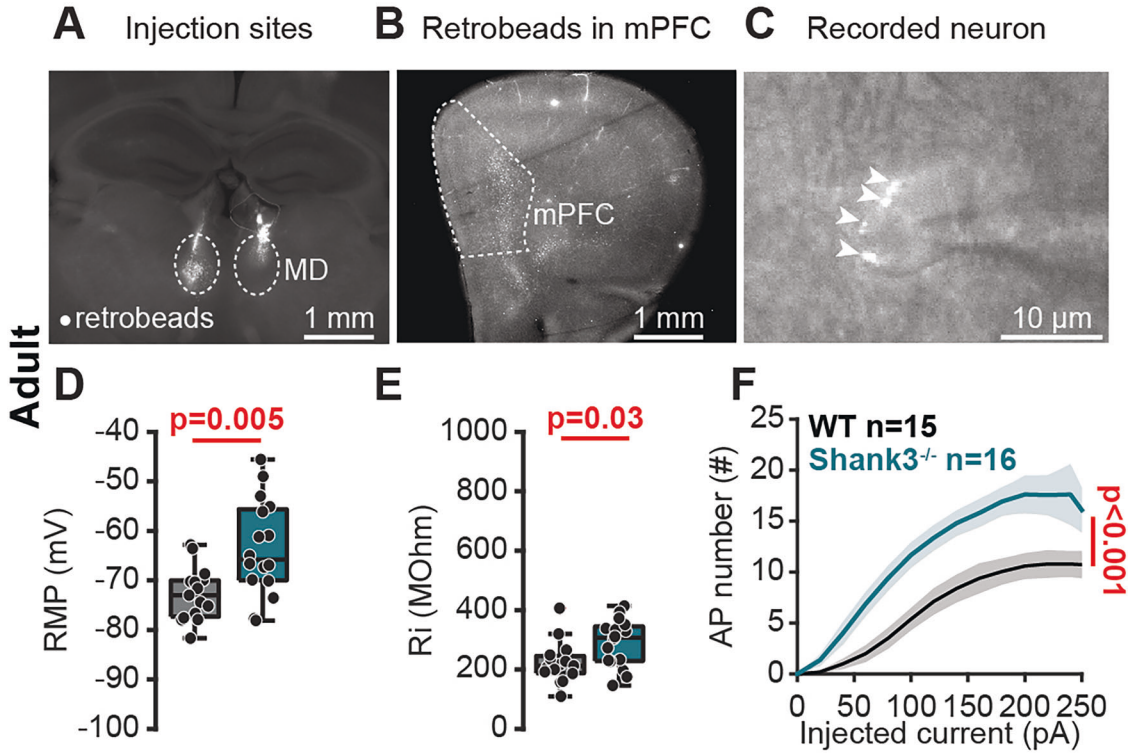


Fig. 4 Electrophysiological properties of retrogradely labeled mPFC layer 5 neurons projecting to the MD thalamus in adults. A Example injection site in the MD thalamus with retrobeads. **B** Retrogradely labeled neurons in the deep layers of the mPFC. **C** Example bead-containing layer 5 neuron recorded with a patch pipette. White arrowheads point to beads. D–E. Box plots summarizing intrinsic properties of adult WT (gray) and Shank3$^{-/-}$ (blue) neurons: resting membrane potential (RMP) **D** and input resistance (Ri) (**E**). **F** Input–output curves showing the number of action potentials elicited during an 800 ms current injection. Solid lines indicate group means, and shaded areas represent error bars (± SEM).

not due to differences in the proportions of pyramidal tract (PT) versus intratelencephalic (IT) neurons between genotypes, we specifically recorded from PT cells retrogradely labeled by bead injections into the MD thalamus a week prior. Because layer 5 pyramidal neurons form the major corticothalamic projection, this approach allowed us to directly test whether hyperexcitability was present in the mPFC–MD pathway. Similar to the global layer 5 population, these mPFC–MD projecting neurons displayed hyperexcitability in adult Shank3$^{-/-}$ mice (Fig. 4) with depolarized resting membrane protocol (Fig. 4D, RMP, WT: −72.8 ± 1.4 vs Shank3$^{-/-}$: −63.5 ± 2.4, p = 0.005, Mann Whitney), higher input resistance (Fig. 4D, Ri, WT: 223 ± 18.2 vs Shank3$^{-/-}$: 289 ± 20.1, p = 0.03, Mann Whitney) and increased numbers of action potentials per depolarizing pulse (Fig. 4F; 2-way ANOVA; genotype p = 0.001, current injection p < 0.0001, interaction p < 0.0001).

Together, these results indicate a developmental shift in excitability across mPFC layers: layer 2/3 pyramidal cells are transiently hypoexcitable in juveniles, while layer 5 pyramidal cells —including those projecting to the MD—develop a persistent hyperexcitability into adulthood.

Decreased E-I ratio observed at P14 and in the adult Shank3$^{-/-}$ mice in mPFC layer 5

A major goal in ASD research has been to find convergent mechanisms in different genetic mouse models. One of the main hypotheses, as proposed by Rubenstein and Merzenich [39], is linking genetic models of autism through a common mechanism of increase in excitatory-inhibitory synaptic ratio. We used whole-cell voltage-clamp recordings to examine the synaptic responses in mPFC layer 2/3 and layer 5 pyramidal cells. Synaptic responses were evoked using al bipolar stimulating electrode placed in upper layer 2/3. Excitatory post-synaptic currents (EPSCs) were recorded across a range of holding potentials between −100 and −30mV (Fig. 3H, traces shown are baseline subtracted responses across this voltage range). From these responses we calculated I/V relationship at the time of maximal synaptic conductance (see Methods), which allowed us to estimate a composite reversal potential value and the corresponding E/E + I value.

The composite reversal potential and excitatory-inhibitory ratio in Layer 2/3 mPFC pyramidal cells were not different between WT and Shank3$^{-/-}$ at either P14 or in adults (Figure S7E-G). By contrast, in layer 5 pyramidal cells from Shank3$^{-/-}$ mice displayed a more negative composite reversal potential and thus a reduced excitatory/(excitatory + inhibitory) ratio already evident at P14 (Fig. 3G-J; mean ± sem; P14, composite reversal potential, WT: −49.7 ± 3.4, P14 Shank3$^{-/-}$: −61.9 ± 3.7, Welch's test, p = 0.03; E/E + I ratio, WT: 0.34 ± 0.04, P14 Shank3$^{-/-}$: 0.2 ± 0.04, Welch's test, p = 0.03) with this reduction in relative contribution of excitation to total synaptic response persisting into adulthood (Fig. 3G-J; mean ± sem; Adults; composite reversal potential, WT: −54.2 ± 2.4, Shank3$^{-/-}$: −65.9 ± 1.85, Welch's test, p = 0.0008; E/E + I ratio, WT: 0.29 ± 0.03, P14 Shank3$^{-/-}$: 0.16 ± 0.02, Welch's test, p = 0.0008).

These data, in contrast to previous observations made in other ASD models, suggest that the imbalance of the E-I ratio in Shank3$^{-/-}$ mice is restricted to inputs to layer 5 pyramidal neurons of the mPFC. Interestingly, this imbalance is observed as early as P14, indicating that these alterations in synaptic function occur during early developmental stages, potentially contributing to the onset and progression of ASD in Shank3$^{-/-}$ mice.

Altered mPFC- MD thalamus synaptic function in Shank3$^{-/-}$ mice

As outlined above, one of the major projections from the deeper layer of mPFC, including the layer 5 pyramidal cells, is the MD

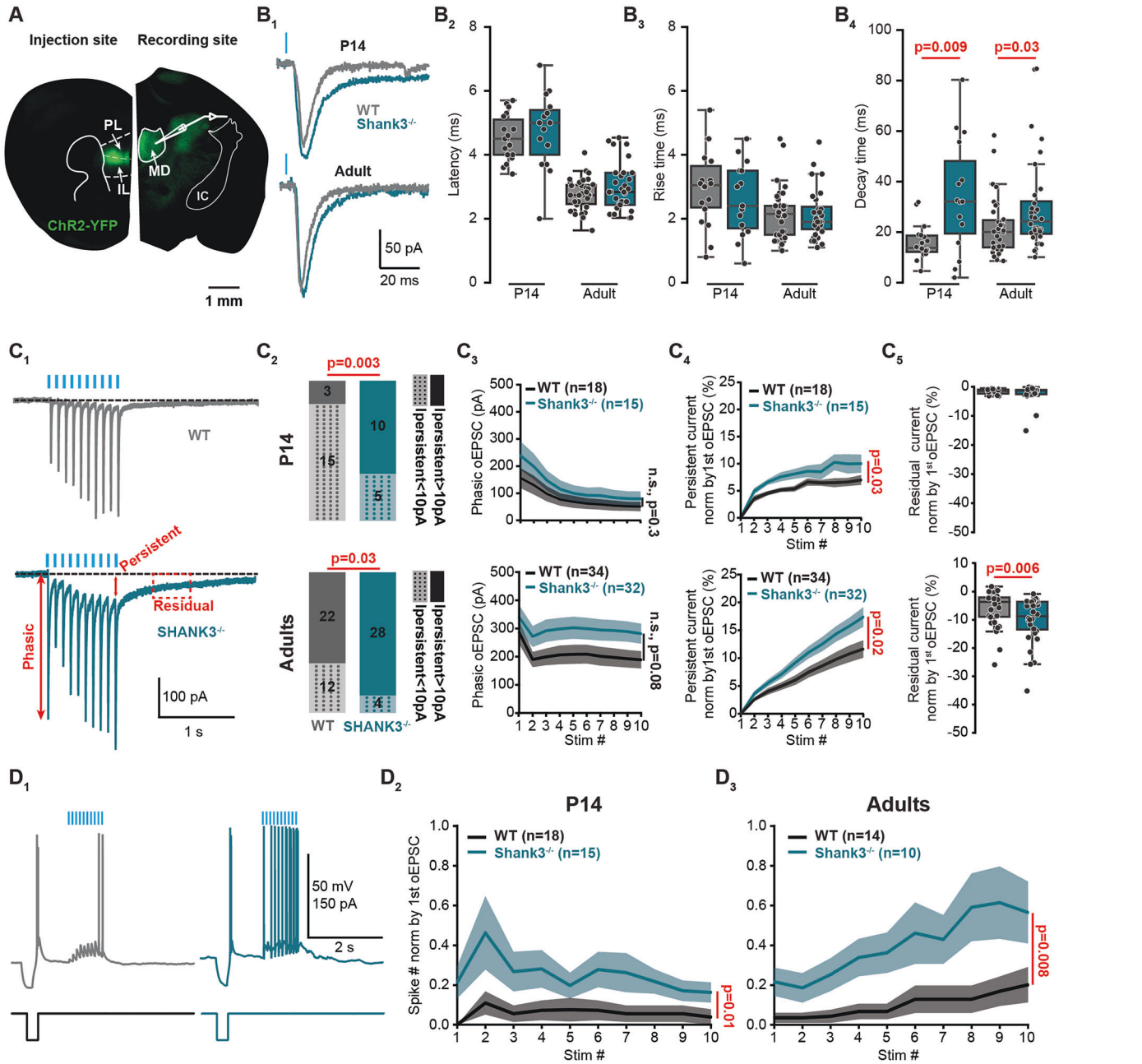


Fig. 5 Enhanced mPFC-MD synaptic function in P14 and adult Shank3$^{-/-}$ mice. A Epifluorescence image showing the injection site of AAV1_ChR2_YFP in mPFC (left) and labeled projections in MD thalamus (right). **B1** Representative optogenetically-evoked EPSC (oEPSC, phasic responses) from MD neurons of WT (grey) and Shank3$^{-/-}$ (blue) mice. Data from P14 animals are shown on the top, while adult data are shown on the bottom. (**B2-B4**) Phasic oEPSC latency, rise time, and decay time for P14 (left) WT (grey, 3 mice, 18 cells) and Shank3$^{-/-}$ (blue, 3 mice, 15 cells), and for adults (right) WT (grey, 16 mice, 34 cells) and Shank3$^{-/-}$ (blue, 12 mice, 32 cells). **C1** Representative oEPSC trains elicited by 10 Hz stimulation. Phasic, persistent, and residual current measurements are indicated in red. Persistent and residual current values are normalized by the amplitude of the first oEPSC in the train. (**C2-5**) P14 (top), Adult (bottom). **C2** Proportions of cells with detectable (>10 pA) or undetectable (<10 pA) persistent current ($I_{persistent}$) in MD cells of WT (grey) and Shank3$^{-/-}$ (blue) mice. **C3** Averaged phasic current amplitude with 10 Hz stimulation for WT (grey) and Shank3$^{-/-}$ (blue) mice. (C4) Averaged persistent current with 10 Hz stimulation for WT (grey) and Shank3$^{-/-}$ (blue) mice. **C5** Residual responses in WT (grey) and Shank3$^{-/-}$ (blue) mice. **D1** Representative traces of current-clamp recordings from MD cells upon repeated activation of mPFC axons. **D2** Number of evoked action potentials during oEPSC trains from P14 WT (black) and Shank3$^{-/-}$ (blue) mice. **D3** Number of evoked action potentials from adult WT (black) and Shank3$^{-/-}$ (blue) mice. The number of evoked action potentials was normalized to the amplitude of the first optogenetically evoked EPSC (oEPSC) recorded during the voltage-clamp train in the same cell. Traces represent mean ± SEM.

thalamus. To evaluate whether the changes we observed in mPFC were associated with and potentially causative of effects on downstream targets, we injected mPFC with one of two Channelrhodopsin2 expressing viruses: AVVDJ for P0 injections (Figure S9) and AAV1 CaMKIIa-ChR2-eYFP for adults, followed by in vivo incubation for several weeks (2 weeks for the pups; 4 weeks minimum for the adults). We then recorded synaptic responses in MD cells (Fig. 5A Figure S8). Shank3$^{-/-}$ MD neurons showed passive properties that were indistinguishable from controls (Figure S8A1-8), suggesting that the changes in intrinsic

excitability we observed were restricted to cortical locations. Using 1 Hz blue light stimulation, we reliably evoked optogenetic monosynaptic excitatory synaptic currents (oEPSCs) as observed with a short and fixed latency (in ms; mean ± sem; P14: WT = 4.5± 0.2; Shank3$^{-/-}$ = 4.8 ± 1.2; Mann Whitney test, p = 0.4; adult: WT = 2.6 ± 0.1; Shank3$^{-/-}$ = 2.9 ± 0.1; Welch's t-test, p = 0.1). oEPSCs showed similar rise time between WT and Shank3$^{-/-}$ (in ms; mean ± sem; P14: WT = 3 ± 0.3; Shank3$^{-/-}$ = 2.6 ± 1.2; Welch's t-test, p = 0.4; adult: WT = 2.2 ± 0.8; Shank3$^{-/-}$ = 2.1 ± 0.8; Mann Whitney test, p = 0.7) but different decay time (in ms; mean ± sem; P14: WT = 16 ± 1.6 ; Shank3$^{-/-}$ = 34.3 ± 5.8; Mann Whitney test, p = 0.009; adult: WT = 22 ± 11.5, Mann Whitney test, p = 0.03; Shank3$^{-/-}$ = 30.2 ± 19, Mann Whitney test, p = 0.03) (Fig. 5B). Thus, mPFC deeper layer efferents generate longer lasting synaptic currents in Shank3$^{-/-}$ MD neurons resulting in an overall greater synaptic charge compared to littermate WT controls. The peak evoked synaptic current amplitudes did not differ between WT and Shank3$^{-/-}$ mice (Figure S8B1-2; FigS10), suggesting that the observed differences in EPSC decay rate were unlikely to be due to any differences in viral efficiency or spread from injection site.

We noticed that during 10 Hz trains, the synaptic current did not fully decay to baseline between individual responses of the train (Fig. 5C). We refer to this build-up as the persistent part of the synaptic response, which accumulates over the course of the oEPSC train. We classified MD neurons regarding whether they showed a persistent response based on the amplitude of the persistent current at the end of the oEPSC train (just before oEPSC #10, Fig. 5C1) greater than 10 pA.

In Shank3$^{-/-}$ mice both the incidence and amplitude and of the persistent synaptic current showed a developmental progression. At P14 only 3/18 WT cells exhibited a persistent current, compared to 10/15 Shank3$^{-/-}$ cells (Fig. 5C2, top, chi-square test, p = 0.003). In adult mice, persistent synaptic responses became more common even in WT mice, appearing in about 2/3 of MD cells (22/34 cells), whereas almost all Shank3$^{-/-}$ MD cells exhibited a persistent current (28/32 cells, Fig. 5C2, bottom, chi-square test, p = 0.03). These results demonstrate a significant difference in the proportion of MD cells showing a late synaptic response between WT and Shank3$^{-/-}$ mice at both P14 and adulthood. Interestingly, in both P14 and adults, the persistent current build-up is greater in Shank3$^{-/-}$ mice than in WT mice Fig. 5C4, top; P14: WT vs. Shank3$^{-/-}$, 2-way ANOVA with repeated measures: genotype p = 0.03; stimulation p < 0.0001; interaction p = 0.06; bottom, Adults: WT vs. Shank3$^{-/-}$, 2-way ANOVA with repeated measures: genotype p = 0.02; stimulation p < 0.0001; interaction p < 0.0001). To control for possible variability in viral transduction, persistent current amplitudes were normalized to the first evoked oEPSC amplitude.

We found that upon termination of oEPSC trains, MD neurons additionally displayed a slowly-decaying "residual" response lasting for several seconds, much longer than the decay time constant of individual oEPSCs reported above (<50 ms). We quantified the residual current as that measured 500 ms following the end of the stimulus train and found that it was greater in Shank3$^{-/-}$ mice, but only in adults (Fig. 5C5; mean ± sem; P14: WT = −1.6 ± 0.2; Shank3–/– = −3 ± 1; Mann-Whitney test, p = 0.8; adults: WT = −5.85 ± 1; Shank3$^{-/-}$ = −9.9 ± 1.4, Mann-Whitney test, p = 0.007). Residual current values were also normalized to the first oEPSC to account for injection-related variability.

Together, these findings indicate increases in connection strength between mPFC and MD neurons in Shank3$^{-/-}$ mice. This synaptic strengthening becomes especially evident during repetitive activation with 10 Hz stimulus trains. Similarly, this repetitive activation at 10 Hz elicited an increase in the number of action potentials of MD cells in Shank3$^{-/-}$ (Fig. 5D1–3, WT vs Shank3$^{-/-}$, 2-way ANOVA with repeated measures, P14: genotype p = 0.009; stimulation p = 0.1; interaction p = 0.6; adults: genotype p = 0.008, stimulation p = 0.004, interaction p = 0.07). Similar to synaptic measures, the number of evoked action potentials was normalized to the first oEPSC amplitude to account for potential differences in viral efficiency.

Synaptic receptors underlying the augmented function of the mPFC-MD synapse in Shank3$^{-/-}$ mice

To investigate the nature of the persistent synaptic current in Shank3$^{-/-}$ mice, we conducted a set of separate experiments in adult mice using pharmacological compounds targeting two major receptor classes known to be affected by Shank3 mutations in other brain regions. Additionally, we chose to target receptors with a long duration of action, based on the previously observed increase in oEPSC decay time and the presence of late persistent current in Shank3$^{-/-}$ mice (Fig. 5). First, we used AP5, an antagonist of NMDA receptors. Second, we conducted an occlusion experiment using DHPG, an agonist of mGluR1 and mGluR5 receptors. These drugs were applied only if the recorded cell exhibited at least 10 pA of persistent current.

We first hypothesized that the increase in persistent current is mediated by NMDARs. Accordingly, bath application of AP5 should induce little to no reduction in WT mice, as oEPSCs recorded at −70 mV are predominantly mediated through AMPARs due to the magnesium block on NMDARs. Consistent with this, 0.1uM AP5 had no significant effect on phasic or persistent currents in WT mice. However, in Shank3$^{-/-}$ mice, AP5 reduced both phasic (Fig. 6A, B ;2 way-repeated ANOVA, bath vs AP5, drug p = 0.009, stimulation p = 0.3, interaction p = 0.9) and persistent current (Fig. 6 A, C;2 way-repeated ANOVA, bath vs AP5, drug p = 0.0001, stimulation p < 0.0001, interaction p < 0.0001), indicating that the Shank3$^{-/-}$ mutation results in abnormal functional activation of NMDARs.

Our second hypothesis, based on the original Shank3$^{-/-}$ complete knockout model [11], is that there is a dysregulation of postsynaptic mGluR5 signaling, which might be expected given that mGluRs show long-lasting responses [40]. We initially tried to use MTEP, the antagonist of mGluR5, but the results were inconclusive. To further investigate, we performed an occlusion experiment using DHPG, a mGluR1 and mGluR5 agonist, reasoning that this would reduce the amplitude of the synaptic response, as a subset of post-synaptic mGluRs would already be activated by bound DHPG. We observed a decrease in both persistent (Fig. 6D, F; 2-way repeated ANOVA, bath vs. DHPG, drug p = 0.003, stimulation p = 0.7, interaction p < 0.0001) and phasic currents (Fig. 6D, E; 2-way repeated ANOVA, bath vs. DHPG, drug p = 0.003, stimulation p = 0.7, interaction p < 0.0001) in Shank3$^{-/-}$ mice, but no change in WT mice. The lack of effect in WT mice suggests that mGluR1/5 signaling is tightly regulated and not recruited at either pre- or postsynaptic sites under normal conditions. In contrast, the reduction in phasic and persistent currents in Shank3$^{-/-}$ mice upon DHPG application likely reflects a dysregulation of mGluR1/5 signaling.

DISCUSSION

In this study, we investigated the pathophysiological development of the mPFC and its output to the MD using the Shank3$^{-/-}$ mouse model of autism spectrum disorder. After initially assessing function at P11, we mainly compared relevant developmental time points, specifically P14 (pre-weaning stage) and adulthood (>P55). Initially, we confirmed known ASD-related behavioral deficits, including impaired social behaviors in adult mice and altered ultrasonic vocalizations (USVs) in juvenile mice. We then employed our in vitro local field potential (LFP) recording design, which allowed us to identify a significant difference in mPFC circuit function between the P14 and adult stages. At P14, we observed hypoexcitability, with a switch to circuit hyperfunction in adults. Furthermore, using whole-cell patch-clamp recordings of pyramidal cells, we uncovered distinct developmental patterns between cortical layers: at P14, layer 2/3 pyramidal cells exhibited

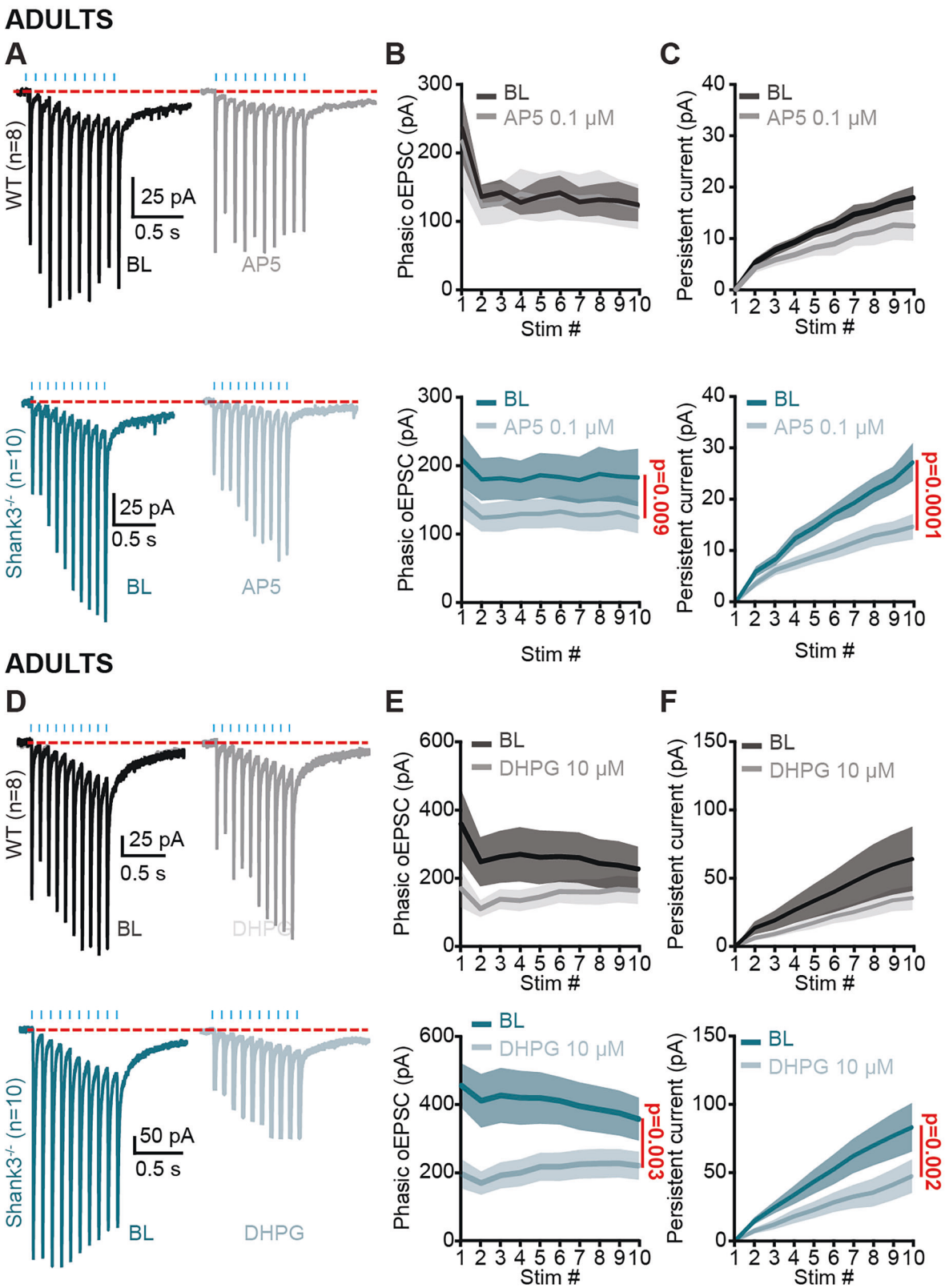


Fig. 6 mGluR and NMDAR contribution to the phasic and persistent mPFC response to oEPSCs in adult Shank3$^{-/-}$ mice. A Representative oEPSCs elicited with 10 Hz stimulation in MD before (dark color) and after 0.1uM AP5 (light color) for WT (grey, 6 mice, 8 cells) and Shank3$^{-/-}$ (blue, 3 mice, 10 cells) mice. **B** Peak amplitude of phasic currents in response to 10 Hz stimulation in WT (top, grey) and Shank3$^{-/-}$ (bottom, blue) mice before (BL, baseline, dark color) and during AP5 bath application (AP5 0.1uM, light color). **C** Same as (**B**) for persistent current. **D** Representative oEPSCs elicited with 10 Hz stimulation in MD before (dark color) and after 10uM DHPG (light color) for MD recordings from WT (grey, 3 mice, 8 cells) and Shank3$^{-/-}$ (blue, 4 mice, 10 cells) mice. **E** MD phasic current with 10 Hz stimulation for WT (top, grey) and Shank3$^{-/-}$ (bottom, blue) mice before (BL, baseline, dark color) and during DHPG bath application (DHPG 10uM, light color). **F** Same as (**E**) for persistent current. Traces are represented are mean (solid line) ± SEM (shaded line).

hypoexcitability, while layer 5 cells showed signs of hyperexcitability. As the mice matured, the hyperexcitability in layer 5 cells was exacerbated, whereas layer 2/3 cells tended to normalize their excitability. Interestingly, we observed that the excitation/inhibition (E/I) ratio was altered specifically in layer 5 neurons at both developmental stages, while no significant changes were observed in layer 2/3 cells. These findings led us to further investigate the mPFC-MD thalamus pathway, a major connection dependent on layer 5 output and involved in social behavior. We observed significant alterations in this pathway, with changes in synaptic strength and post-synaptic receptor composition in Shank3$^{-/-}$ mice, which were linked to disruptions in NMDA and mGluR group 1 receptor signaling.

Longitudinal approaches in ASD research

While much ASD research focuses on mature animals, longitudinal studies are critical for understanding how genetic mutations influence neurodevelopment. Our study highlights the progression of deficits in Shank3$^{-/-}$ mice, starting with early behavioral alterations at P11 and cellular hypoexcitability at P14, which then evolves into circuit hyperfunction in adulthood. The observed shift in mPFC network activity across development, from hypoexcitability to hyperfunction, is to our knowledge a completely novel finding. Observations of early cellular deficits have been reported in other studies using a different Shank3 mutant model, Shank3B$^{-/-}$, in the corticostriatal circuit, where early abnormal hyperactivity of corticostriatal afferents was observed [41], however the long-term changes into adulthood were not reported. This group also confirmed early behavioral alterations in the Shank3B$^{-/-}$ model [42]. Altered USVs are also commonly observed in various genetic mouse models of ASD [10]. These observations suggest that longitudinal approaches, such as our work, can provide critical insights into how gene mutations influence the progression of ASD over time and might help reveal potential targets and windows for therapeutic intervention.

Layer-Specific mPFC Excitability in ASD

As mentioned above we found layer specific mPFC deficits that are different at P14 compared to the adults. The scientific literature regarding mPFC dysfunction has largely focused on mature animals [5, 24, 43, 44]. The hyperexcitability observed in mPFC layer 5 pyramidal cells is consistent with findings in other mouse model [5, 36, 45]. However, other reports suggest that mPFC layer 2/3 cells can be altered in genetic mouse ASD models [31, 44]. Our intracellular recording data (Fig. 3) revealed that while the intrinsic properties of layer 2/3 pyramidal cells are comparable between adult Shank3$^{-/-}$ and WT mice, layer 5 pyramidal cells exhibit hyperexcitability in Shank3$^{-/-}$ mice. Consistent with this, when we selectively targeted mPFC neurons projecting to the MD using retrobead labeling, we found that adult Shank3$^{-/-}$ layer 5 projection neurons were hyperexcitable compared to WT. A novel finding of our study is that these properties appear to be dynamic and development-dependent. Specifically, we detected hypoexcitability in layer 2/3 cells at P14, while layer 5 cells exhibited only a mild hyperexcitability—characterized by a depolarized resting membrane potential—at this stage. We speculate that compensatory mechanisms may normalize layer 2/3 cell excitability by adulthood, while at the same time this could, through enhanced output, lead to hyperexcitability in layer 5 cells in adult mice. Pyramidal cell morphology and intrinsic membrane properties develop in parallel in layers 2/3 and 5; however, the development of synaptic inputs differs between these layers [46] : during the first two postnatal weeks, layer 2/3 primarily receives excitatory inputs, while layer 5 does not [47]. Shank3 is a scaffolding protein found in excitatory synapses [48, 49]. Its knockout may first affect early-developing synapses in layer 2/3 before impacting those in layer 5. This suggests that different layers of the mPFC may be affected differently to different ASD- related gene mutations.

Taking advantage of simultaneous recordings across layers with our in vitro multi-electrode array assay (Fig. 2), we recorded LFP/CSD signals reflecting synaptic activity in mPFC neurons. Comparable to our patch-clamp data, we observed an interesting dynamic of signal excitability depending on age. At P14, we discovered that only the presynaptic signal (fiber volley) in layer 5 is hypoexcitable. This signal reflects a combination of both subcortical inputs, including thalamic, as well as intracortical inputs, including those arising both locally and distally. Recent studies have highlighted the importance of MD thalamus projections to layer 5 of the mPFC, showing that artificially reducing activity in this pathway during a critical developmental period can lead to behavioral deficits in adulthood [50]. In line with this, our retrobead recordings further suggest that hyperexcitability of adult Shank3$^{-/-}$ corticothalamic neurons may contribute to long-term circuit dysfunction in this pathway. Similarly, we demonstrate that in a mutant model of autism, hypoexcitability of the fiber volley component at P14 may also serve, at least in part, as an early indicator of future adult behavioral deficits. In adulthood, we observed a global presynaptic hyperfunction of the mPFC across both layers, with layer 5 postsynaptic signals also hyperfunctional. Our results highlight the heterogeneity of ASD-related neurodevelopmental changes, where distinct mPFC layers and synaptic circuits exhibit alterations at different developmental stages. Consequently, these findings underscore the importance of considering both layer-specific and age-dependent parameters when studying the pathophysiological mechanisms linked to ASD.

E/I ratio theory in ASD

Twenty years ago, Rubenstein and Merzenich hypothesized that ASD dysfunction may generally be related to increase in excitatory/ inhibitory ratio [39]. This theory has been of interest of many [8, 50] as it can relate to different ASD mouse models. Recently, Antoine et al. [51] has observed an elevated E-I ratio is a common circuit phenotype in four different genetic mouse models of ASD. They demonstrated that this elevation reflects stabilization of synaptic drive rather than driving network hyperexcitability, as was previously believed. In contrast, in our study (Fig. 4), we observed a reduction in the E/I ratio in Shank3$^{-/-}$ mPFC layer 5 cells at both P14 and in adults. Despite this, LFP recordings revealed global mPFC hyperfunction and layer 5 pyramidal neuron hyperexcitability in adults, though less so at P14. These results do not directly contradict the findings of Antoine et al. but suggest that the E/I ratio imbalance as observed at the single cell level may not necessarily be the cause of the observed network excitability changes. Instead, the reduced E/I ratio we observed may reflect an adaptive response to early cellular-level disruptions, possibly originating from developmental imbalances that influence network function later. Additionally, at this point we cannot exclude potential changes in interneuron excitability, as Shank3$^{-/-}$ models have been shown to exhibit deficits in interneuron function, which could also contribute to the observed network alterations [52, 53].

mPFC-MD synaptic connectivity

Both P14 and adult Shank3$^{-/-}$ mice exhibit altered mPFC-MD thalamus synaptic connectivity which results in a functional increase in mPFC-driven MD neuron spikes (Fig. 5). Additionally, we observed a greater incidence of persistent and residual synaptic responses in MD neurons of adult Shank3$^{-/-}$ mice which may contribute to behavioral dysfunction. In agreement with our observation of altered corticothalamic connectivity, it has been shown that sensory cortico-thalamic synapses are also altered in adults Shank3$^{-/-}$ mice [54], also displaying a buildup of current under a 40 Hz train stimulation.

Clues for a critical period of development for the mPFC-MD circuit have emerged. Indeed, anatomical lesions [55] or chemogenetic modulation to disturb the mPFC-MD circuit before adulthood results in physiological changes of mPFC activity [56, 57] or social behavior [56]. Similar modulation in adulthood failed to affect mPFC circuits or social behavioral changes. It is interesting to note that the density of connections between the mPFC and MD regions decreases at postnatal day 14 (P14) [12] and that a similar decrease in the expression of the SHANK3 transcript occurs at the same time point [19]. Our findings emphasize significant alterations in mPFC-MD synaptic connectivity in Shank3$^{-/-}$ mice, with functional changes evident across both juvenile and adult stages. The increased incidence of persistent synaptic responses in adult mice underscores the lasting impact of these early disruptions, highlighting the need to further understand how such changes contribute to behavioral dysfunction.

Importantly, the choice of NMDA and mGluR pharmacological manipulations was motivated by the longer decay times observed in MD cells of Shank3$^{-/-}$ mice (Fig. 5CB4). This observation led to several mechanistic hypotheses, including receptor mislocalization [11], spillover effects [58], altered receptor composition [59, 60], or an incomplete developmental switch [61]. Interestingly, pharmacological modulation affected the persistent component in Shank3$^{-/-}$ mice but had no detectable impact on WT, suggesting that NMDARs and mGluRs are indeed potential targets for this buildup of current in Shank3$^{-/-}$ mice (Fig. 6). In our study, we observed a novel population difference in the presence of persistent currents between Shank3$^{-/-}$ and WT mice. Specifically, at both P14 and in adulthood, a majority of cells from Shank3$^{-/-}$ mice displayed persistent currents (67% at P14; 88% in adults), whereas WT mice showed a much lower proportion at P14 (17%) and a moderate increase in adulthood (65%) (Fig. 5).This finding is consistent with the known alterations in NMDA receptor-mediated neurotransmission in other Shank3 loss of function models [56, 62], where NMDA signaling is disrupted. Additionally, the occlusion experiment with DHPG provided further insight into the altered receptor signaling in Shank3$^{-/-}$ mice. DHPG application led to also to a reduction in phasic current, suggesting that presynaptic alterations could contribute to the phenotype. Collectively, these findings reinforce the notion that Shank3 deficiency leads to disruptions in both NMDA and mGluR1/5 signaling pathways, ultimately affecting synaptic transmission.

Caveats and limitations

Here we demonstrated novel findings of developmental ASD-related circuit dysfunction in a model of severe ASD, Shank3$^{-/-}$ mice, at two important time points: P14 and adults (>P55). However, a potential limitation of our results is that they were mainly obtained in isolated brain slices. These have the advantage of being accessible for mechanistic and pharmacological characterization, using LFP or cellular physiology. However, the conditions in vitro can never completely match those in the intact brain, and any disease-related differences in extrinsic connectivity, neuromodulatory state, etc. will not be directly revealed by the in vitro approach. Yet the use of in vitro optogenetics and pharmacology has the advantage of leading to better understanding of cellular/molecular pathophysiological mechanisms directly related to genetic mutations. It is also important to acknowledge that the Shank3$^{-/-}$ model is a homozygous knockout, and not a heterozygous mutation as seen in most human cases. As such, it may not fully recapitulate the complexity of human *Shank3* mutations or their phenotypic variability. Nevertheless, it remains a widely used [63, 64] and valuable tool for studying synaptic mechanisms relevant to ASD, particularly due to the central role of SHANK3 in excitatory synapse structure and function. One additional potential drawback of LFP network analysis is that the mode of synaptic stimulation is through single extracellular stimulus pulse that evokes a simplified and highly synchronized input that may not model normal ongoing circuit activity in behaving animals. Yet being able to reliably and quantitatively determine input-output relationships provides an integrated and robust assay of circuit excitability and E/I ratio that together outweigh this limitation. Further, given that both WT and Shank3$^{-/-}$ slices received comparable stimulation, yet displayed different responses, with hyperfunction of mPFC observed in adult Shank3$^{-/-}$, it indicates that the circuit state in Shank3$^{-/-}$ is more sensitive to synaptic input than in the WT.

It would be interesting in the future to perform similar experiments in vivo by for example optogenetically stimulating the MD thalamus axon in mPFC while recording mPFC activity with linear silicon multielectrode probes. Another limitation of our study is that as of now, there is no direct evidence of a link between early circuit dysfunction and later behavioral effects. Future studies, using in vivo recording, like fiberphotometry [65] or miniscope [26] during the social interaction task will allow to relate the activity of mPFC (bulk fiberphotometry signal) or mPFC cells (miniscope) to the deficits. Finally, our recordings in layer 5 initially targeted the global pyramidal cell population without distinguishing between intratelencephalic (IT) and pyramidal tract (PT) neurons. Classical criteria for identifying these subtypes [5, 66] —based on dendritic morphology or intrinsic physiological signatures such as H-current, sag ratio, or firing adaptation—were not applicable here, as biocytin labeling did not reliably capture the full set of recorded neurons, and Shank3 knockout altered both morphology and intrinsic properties, complicating classification. To refine our conclusions, we used retrobeads labeling to selectively identify MD-projecting PT neurons and confirmed that these cells were hyperexcitable in adult Shank3$^{-/-}$ mice.

It is also possible that our MD-mPFC optogenetic experiments may have engaged both layer 5 and layer 6 projection neurons [67], as the viral injections cannot be strictly confined to layer 5. While we observed similar proportions of synaptic facilitation and depression in both genotypes, the specific effects of DHPG were differentially modulated in Shank3$^{-/-}$ slices. This effect in Shank3$^{-/-}$ mice may reflect altered contributions from layer 5 and layer 6 corticothalamic inputs, which give rise to 'driver' and 'modulator' synapses, respectively. Layer 5-derived driver synapses typically convey strong, fast signals with minimal modulation, whereas layer 6-derived modulator synapses exert more subtle regulatory control over thalamic activity and are more sensitive to metabotropic modulation, such as by mGluRs. The differential effects of DHPG observed in Shank3$^{-/-}$ mice could thus be related to an imbalance or functional change in these two types of inputs.

Conclusions and future directions

This study uncovers a critical and never described shift in mPFC network activity in Shank3$^{-/-}$ mice with distinct layer-specific alterations. Our findings highlight the progressive nature of ASD-related cortical dysfunction, emphasizing disruptions in the mPFC-mediodorsal thalamus pathway as a potential link to behavioral deficits. Crucially, this research underscores the importance of developmental timing in ASD, suggesting that early circuit dysfunction may set the stage for long-term impairments. By identifying these critical windows, our work lays the foundation for targeted early interventions, opening new possibilities for mitigating ASD-related neurodevelopmental disruptions.

Our study can serve as a starting point for establishing a causal link between early neurodevelopmental events and ASD-relevant neural circuit alterations. Acute mPFC circuit manipulation using optogenetics [65] or chemogenetics [56, 68] in adults has been shown to be able to rescue some social behavior. It will be interesting to see if similar manipulations performed chronically during early life will have a significant impact on adult physiology and behavior. By identifying these critical periods of mPFC

development, we might be able to perform early interventions that may prevent or mitigate ASD-related circuit dysfunction.

MATERIALS AND METHODS

Animals

Mice were bred and maintained according to Stanford University, School of Medicine Animal Research Requirements, and all procedures were approved by the Committees on Animal Research at Stanford University (protocol number: 12363). Mice carrying the *Shank3* complete knock out (Δe4–22) were a kind gift from Dr. Yong-Hui Jiang [11], Duke University. All comparisons were made using both genders. Mice used for experiments were separated in two distinct age group: P14 (+/- ½ day) and adults (2–4 months). The mice were maintained on a 12 hr light/dark cycle. Food and water were available ad libitum.

Genotyping of transgenic animals

Shank3$^{-/-}$ and Shank3 WT mice were genotyped by PCR using the following primers: wild-type forward GTGCCACGATCTTCCTCTAAAC, wild-type reverse, AGCTGGAGCGAGATAAGTATGC, mutant forward TTGCAT CTGGGACCTACTCC and mutant reverse AAAGCACTGACTCCTCTCTTGG. Experimenters were blinded to data acquisition and analysis whenever possible. This was the case for all main sets of adult experiments. However, additional adult mice were added later to balance group sizes and were not blinded (see Fig. 6; the imbalance in the number of WT cells showing persistent current was apparent). Exceptions were also made for pup extracellular and patch-clamp experiments, where the genotype was determined in the lab by the experimenters. For the P11 behavioral experiments, experimenters remained blinded until the completion of the analysis, as entire litters were tested together.

Based on our previous experience, we determined that for extracellular recordings, a minimum of 3 mice per group with 3 slices per mouse was sufficient to detect statistical differences. For electrophysiology experiments, at least 3 mice per group with 5 cells per mouse were deemed necessary. For new experiments, such as optogenetics and behavioral studies, we performed power calculations to determine the appropriate sample sizes. After completing preliminary datasets, we conducted power analyses to refine our sample size estimates. The required number of samples was calculated based on the observed effect size (Cohen's d), using an alpha level of 0.05 and a statistical power of 80%.

Behavioral tests

Ultrasonic vocalization recordings. Ultrasonic vocalizations are typically emitted by pups from birth to the weaning period and are related to communication behavior. In this study, we elicited ultrasonic vocalizations (USVs) by isolating the pups briefly from their dams and littermates [69]. Specifically, one hour before the recordings, on postnatal day 11 (P11) the breeders were removed from the home cage. The home cage with the remaining litter was then moved to the testing room and placed on a heating pad for one hour to maintain the body temperature. Pups were then individually isolated. Each tested pup was placed in a testing cage within a sound-isolated, darkened box, with an UltraSoundGate 116Unb recording system (Avisoft Bioacoustics) positioned 15 to 20 cm above. The USVs were recorded with a sampling rate of 384,000 Hz in a 16-bit format (recording range: 0–250 kHz) for 10 minutes using the Avisoft-RECORDER USG/USGH software. Finally, the pup was returned to its home cage with its littermates. Once the entire litter had been tested, the home cage was returned to its original room, and the breeders were placed back in the cage. The recordings were next analyzed using the Avisoft-SASLab Pro software (version 5.3.2–14; Avisoft Bioacoustics). In recordings of pup vocalizations over a 10-minute period, the first 2 minutes are excluded from analysis as the calls may result from handling-related stress. Fourier transformation (512 pt FFT, Frame=100%, Hamming window with 75% of time overlap) was applied to obtain the spectrograms (500 Hz: Frequency resolution; 0.5 ms: Time resolution). USV detection was performed using automatic whistle tracking in SASLab. Monotonic calls with a minimal duration of 5 ms and slope of −15 to 6 kHz/ms were counted. Number of calls was tested for Normality using a Shapiro-Wilk test. Between-group comparison was performed using a non-parametric Mann Whitney test. Data are reported as mean + /- sem.

Ultrasonic vocalizations were classified manually in 11 categories using categories based on previously published classifications [70]. A chi-square test was used to compare the overall distribution of USV types between genotypes. To determine which specific USV categories contributed to the group differences, a post hoc analysis was performed using the standardized residual method. The standardized residual for each cell was calculated as: Standardized Residual = (Observed – Expected) / √Expected. Significant deviations from expected frequencies are indicated by asterisks based on their corresponding p-values.

Social preference test. To measure sociability, mice were tested in a social interaction task. A clean box was partitioned into three zones. A camera was mounted directly above the box to record videos that were analyzed offline. Tested mice were habituated to the empty box for ten minutes, the first day. The next day, a pre-test phase was performed using two empty cages, one at each end of the box. The tested mouse had 10 minutes to explore. The test phase is performed 10 minutes later. A novel object was placed within a perforated cage at one end of the box and a conspecific is placed in a cage at the opposite end. The placement of the novel object and never-met mouse was randomly assigned. Using EzTrack [71], the videos were scored to determine mouse position, including time spent in regions of interest (ROIs) drawn around the cage containing either the novel object or the conspecific. After checking for normality, the interaction time between an inanimate object or conspecific was tested using a Welch's t-test.

Extracellular multielectrode recordings

Extracellular recordings were performed on coronal neocortical 400 µm thick slices from P14 or adults (>P55) Shank3$^{-/-}$or Shank3 wild type (WT) containing the medial prefrontal cortex (mPFC). Slices were recorded in a humidified oxygenated interface chamber at 34 °C and perfused at a rate of 2 ml/min with oxygenated artificial cerebrospinal fluid (aCSF). The aCSF contained (in mM): 10 glucose, 26 $NaHCO_3$, 2.5 KCl, 1.25 $NaHPO_4$, 1 $MgSO_4$, 2 $CaCl_2$, and 126 NaCl (300 mOsm).

A linear silicon multichannel probe (16 channels, 100 µm inter-electrode spacing, NeuroNexus Technologies) was positioned normal to the medial surface and spanning across all layers of the mPFC to record evoked local field potentials (LFPs). The silicon probe was linked to a pre-amplifier (PZ5-32, Tucker-Davis Technologies (TDT)), and recordings were made using an RZ5D processor (TDT). Data acquisition was conducted using the Real-time Processor Visual Design Studio (RPvdsEx) tool and a custom Python code. LFP data were acquired at 25 kHz and filtered between 0.1 and 500 Hz. A bipolar tungsten microelectrode (each wire, 50–100 kΩ, FHC) positioned in upper layer 5 was used to deliver a bipolar electrical stimulation (0.1 ms duration, intensity loops from 100 to 800 µA, interval of 15 s). In order to obtain a more reliable index of the location, direction, and magnitude of currents underlying network activity, we derived the current-source density (CSD) from raw LFP signals [27]. Assuming a uniform extracellular resistivity, the CSD can be estimated as the second spatial derivative of the LFP. In our experiment, CSD was computed in mPFC by algebraic differentiation of the LFP at adjacent electrodes in the linear probe spaced by 100 µm and assumed a uniform extracellular resistivity of 0.3 S/m [72]. In addition, the following drugs, DNQX (AMPAR antagonist; 25uM) and CPPene (SDZ EAA 494; NMDA competitive antagonist; 1 µM) were applied in the bath to identify the pre and post synaptic component of our signals. Relevant components were next identified based on their distinct shape and their amplitude was measured for each slice. Between-group comparison was performed using a 2-way repeated measure ANOVA. Data are reported as mean + /- sem.

Electrophysiological whole-cell patch-clamp recordings in mPFC slices

Mice were deeply anesthetized with isoflurane (for P14 mice) or pentobarbital sodium (i.p., 50 mg/kg; for adult mice). P14 mice were directly decapitated. Adult mice were perfused transcardially with ice-cold (4 °C), oxygenated (95% O_2 /5% CO_2) sucrose aCSF slicing solution containing (in mM): 234 sucrose, 11 glucose, 26 $NaHCO_3$, 2.5 KCl, 1.25 NaH_2PO_4, 10 $MgSO_4$, and 0.5 $CaCl_2$ (310 mOsm). Brains were quickly removed and 250 µm-thick coronal slices of mPFC cortex were cut in sucrose solution using a vibratome (VT1200; Leica). Slices were transferred to a holding chamber filled with standard ACSF bubbled with 95% O_2 and 5% CO_2. The composition of aCSF was (in mM): 10 glucose, 26 $NaHCO_3$, 2.5 KCl, 1.25 $NaHPO_4$, 1 $MgSO_4$, 2 $CaCl_2$, and 126 NaCl (300 mOsm). Slices were allowed to recover 30 minutes at 37 °C and were then incubated at room temperature (20–25 °C) until recording.

Individual slices were transferred to a recording chamber and continuously perfused at 2 ml/min with oxygenated aCSF at room temperature. Patch pipettes (3–5 MΩ) were pulled from borosilicate glass (Sutter Instrument, CA, USA) on a micropipette puller (Model P1000, Sutter Instrument, CA, USA) and filled with an intracellular solution containing (in mM): K-gluconate, 144; $MgCl_2$, 3; HEPES, 10; EGTA, 0.5 and 2 mg/ml biocytin, pH= 7.2, 280 mOsm. Whole-cell patch-clamp recordings were obtained from layer 2/3 or layer 5 pyramidal cells selected based on their morphology and electrophysiological profile. Layer 2/3 cells were visually distinguishable from layer 5 cells as a thin, densely packed band of somata located near the pial surface. Recordings were performed at room temperature (20–25 °C) using a patch-clamp amplifier (Multiclamp 700B, Molecular Devices) connected to a Digidata 1440 A interface board (Molecular Devices). Signals were amplified and collected using pClamp 10.7. Cells with a stable access resistance of <25MΩ were analyzed. Resting membrane potential was measured immediately upon obtaining the whole-cell configuration, and only cells with a resting membrane potential more hyperpolarized than −50 mV were selected. Resting membrane potential was computed as the average of the sweeps were no current was injected. Membrane potentials were not corrected for junction potential. Cells were held at their resting membrane potential and V/I curves were constructed from a series of 800 ms current steps in 10pA and 20pA increments. Input resistance was determined from the slope of the V/I curve in the linear region within 5 mV of the resting membrane potential. Rheobase was calculated as the minimal depolarizing current step triggering an action potential.

To measure evoked excitatory (E) and inhibitory (I) currents with a potassium gluconate–based internal solution, we first determined the stimulus intensity by recording responses at −70 mV. Stimulus intensity was gradually increased to the maximum value that evoked a synaptic response, but did not trigger action potentials. To estimate the balance of excitatory versus total synaptic activity, we kept stimulus intensity constant and obtained synaptic current responses across a range of voltage-clamp membrane potentials between −100 mV to −30 mV. The net synaptic current was obtained by subtracting the baseline (pre-stimulus current level) from the overall current response, examples are shown in Fig. 3H. We developed an index of excitatory/inhibitory evoked response by using linear fits to estimate the synaptic conductance and reversal potential (E_{rev}) [73] at multiple time points during the evoked response, every 2 ms, following the stimulus onset. To standardize the measure we report the composite E_{rev} calculated at the time of maximum synaptic conductance. Assuming values of −80 for inhibitory E_{rev} and + 10 mV for excitatory E_{rev}, we can calculate the contribution of excitatory conductance to the total synaptic conductance (E/E + I) where a value of 1 would mean no contribution from inhibition, a value of 0 indicating no contribution from excitation, and a value of 0.5 meaning equal contributions from inhibition and excitation. Sweeps with action potentials or nonlinear baseline drifts were excluded from analysis, and only cells with well-fitted linear I/V curves ($R^2 > 0.8$) were retained. To validate this approach, we obtained a complementary data set recording with a cesium-based internal solution. Cells were held at −70 mV to record excitatory synaptic currents (EPSCs) and, using the same stimulus intensity, at + 10 mV to record inhibitory synaptic currents (IPSCs). The peak amplitudes of these responses were used to calculate a direct excitatory–inhibitory ratio (E/I). Results are given as mean ± standard error of the mean (sem). Between-group comparisons were performed using parametric test. A p-value below 0.05 was considered statistically significant.

After recordings, slices were fixed overnight at 4 °C in 4% paraformaldehyde/ PBS and then washed in PBS. Slices were processed using Alexafluor 488-conjugated streptavidin (1:500, Invitrogen) to reveal biocytin. After a series of wash in PBS, slices were mounted on gelatin-coated slides in Fluoromount-G for confocal microscopy.

Morphological analysis

Zeiss LSM900 laser scanning confocal microscope was used to image the mPFC layer 5 biocytin labelled neurons with 63x objectives and a 488 nm laser. Images were processed using ImageJ (National Institutes of Health; http://rsbweb.nih.gov/ij/). Neuronal tracing and analysis were performed using the SNT toolbox [74].

Viral injections

For adult experiments, the procedure for viral injection has been described in detail [75]. Briefly, young adult mice were anesthetized using isoflurane (3% induction, 1.5% maintenance) and received carprofen 5 mg/kg intra peritoneal injection. Mice received bilateral injection in mPFC (in mm from bregma, AP 1.8, ML + /−0.5, DV −2.6). A volume of 500 nl of virus encoding the ChR2 (AAV1-CaMKIIa-ChR2(H134R)_eYFP-WPRE-HGH, 10^{12} GC, 100 nl/min, Penn Vector Core, Addgene 26969 P) was delivered to the injection sites.

For P14 recordings, P0 mice were anesthetized on ice. Mice received a bilateral injection in the frontal area (in mm from lambda, AP: 3.5, ML: + /−0.1, DV:−1.5). A volume from 100 to 200 nl of virus encoding the ChR2 (AAVDJ-CaMKIIa-ChR2(H134R)_eYFP, 10^{12} GC, 100 nl/min, Gene Vector and Virus Core at Stanford University, catalog #36) was delivered to the injection sites.

Optogenetics experiments

ChR2-expressing mPFC axons to MD thalamus neurons were activated using blue LEDs stimulations (Thorlabs M450LP2, 450 nm, duration 1 ms, maximal light intensity 13 mW, 19 mW/cm2) or blue laser (Laserglow Technologies, 473 nm, duration 1 ms, maximal light intensity 8 mW, 10.8 mW/cm2). The mPFC-MD thalamus synaptic connection was evaluated using 10 light stimulations at both 1 Hz and 10 Hz, with one train administered every 20 seconds, while maintaining voltage clamp at −70mV. The resultant synaptic responses were evaluated in voltage clamp to measure synaptic current and in current clamp to quantify the number of action potentials. Synaptic properties parameters were measured using custom MATLAB code.

To investigate the receptor composition underlying the abnormal persistent current observed in adult $Shank3^{-/-}$ mutant mice, either DL-2-Amino-5-phosphonovaleric acid (AP5, Sigma, A5282) at a concentration of 100 µM (broad-spectrum NMDA receptor blocker) or (RS)-3,5-Dihydroxyphenylglycine (DHPG, Tocris, #0342) at a concentration of 10 µM (selective group I mGluR agonist) were applied for 10 minutes in the bath after obtaining a stable baseline recording. Baseline noise was quantified across all recorded cells (n = 67), yielding a mean standard deviation of 2.7 pA; to ensure conservative detection, a threshold of three times this value (8.2 ± 1.3 pA) was applied, and persistent currents were defined as responses exceeding 10 pA. Partial washout was obtained in some cases. The impact of AP5 and DHPG on the 10 Hz voltage-clamp synaptic response was quantified and compared to the baseline recordings. Statistical analysis, 2-way ANOVA with repeated measure, was performed to evaluate the significance of the effects observed. A Grubbs' test with an alpha threshold of 0.05 was used to identify and remove a potential outlier in the adult evoked spiking dataset.

DATA AVAILABILITY

Data have been uploaded and deposited in Dryad (DOI: 10.5061/dryad.zcrjdfnsm).

REFERENCES

1. Wetherby AM, Woods J, Allen L, Cleary J, Dickinson H, Lord C. Early indicators of autism spectrum disorders in the second year of life. J Autism Dev Disord. 2004;34:473–93.
2. De Giacomo A, Fombonne E. Parental recognition of developmental abnormalities in autism. Eur Child Adolesc Psychiatry. 1998;7:131–6.
3. Hodel AS. Rapid infant prefrontal cortex development and sensitivity to early environmental experience. Developmental Rev. 2018;48:113–44.
4. Sato M, Nakai N, Fujima S, Choe KY, Takumi T. Social circuits and their dysfunction in autism spectrum disorder. Mol Psychiatry. 2023;28:3194–206.
5. Brumback AC, Ellwood IT, Kjaerby C, Iafrati J, Robinson S, Lee AT, et al. Identifying specific prefrontal neurons that contribute to autism-associated abnormalities in physiology and social behavior. Mol Psychiatry. 2018;23:2078–89.
6. Luo Y, Wang L, Cao Y, Shen Y, Gu Y, Wang L. Reduced excitatory activity in the developing mPFC mediates a PVH-to-PVL transition and impaired social cognition in autism spectrum disorders. Transl Psychiatry. 2024;14:1–14.
7. Amodio DM, Frith CD. Meeting of minds: the medial frontal cortex and social cognition. Nat Rev Neurosci. 2006;7:268–77.
8. Yizhar O, Fenno LE, Prigge M, Schneider F, Davidson TJ, O'Shea DJ, et al. Neocortical excitation/inhibition balance in information processing and social dysfunction. Nature. 2011;477:171–8.
9. Lee E, Rhim I, Lee JW, Ghim JW, Lee S, Kim E, et al. Enhanced neuronal activity in the medial prefrontal cortex during social approach behavior. J Neurosci. 2016;36:6926–36.
10. Lai JKY, Sobala-Drozdowski M, Zhou L, Doering LC, Faure PA, Foster JA. Temporal and spectral differences in the ultrasonic vocalizations of fragile X knock out mice during postnatal development. Behav Brain Res. 2014;259:119–30.

11. Wang X, Bey AL, Katz BM, Badea A, Kim N, David LK, et al. Altered mGluR5-Homer scaffolds and corticostriatal connectivity in a Shank3 complete knockout model of autism. Nat Commun. 2016;7:11459.
12. Klune CB, Jin B, DeNardo LA. Linking mPFC circuit maturation to the developmental regulation of emotional memory and cognitive flexibility. eLife. 2021;10:e64567.
13. Kolk SM, Rakic P. Development of prefrontal cortex. Neuropsychopharmacol. 2022;47:41–57.
14. Ferguson BR, Gao WJ. Development of thalamocortical connections between the mediodorsal thalamus and the prefrontal cortex and its implication in cognition. Front Hum Neurosci. 2015;8:1027.
15. Verpelli C, Dvoretskova E, Vicidomini C, Rossi F, Chiappalone M, Schoen M, et al. Importance of Shank3 protein in regulating metabotropic glutamate receptor 5 (mGluR5) expression and signaling at synapses. J Biol Chem. 2011;286:34839–50.
16. Moessner R, Marshall CR, Sutcliffe JS, Skaug J, Pinto D, Vincent J, et al. Contribution of SHANK3 mutations to autism spectrum disorder. Am J Hum Genet. 2007;81:1289–97.
17. Boccuto L, Lauri M, Sarasua SM, Skinner CD, Buccella D, Dwivedi A, et al. Prevalence of SHANK3 variants in patients with different subtypes of autism spectrum disorders. Eur J Hum Genet. 2013;21:310–6.
18. Delling JP, Boeckers TM. Comparison of SHANK3 deficiency in animal models: phenotypes, treatment strategies, and translational implications. J Neurodev Disord. 2021;13:55.
19. Waga C, Asano H, Sanagi T, Suzuki E, Nakamura Y, Tsuchiya A, et al. Identification of two novel *Shank3* transcripts in the developing mouse neocortex. J Neurochem. 2014;128:280–93.
20. Rios O, Villalobos J. Postnatal development of the afferent projections from the dorsomedial thalamic nucleus to the frontal cortex in mice. Developmental Brain Res. 2004;150:47–50.
21. Peça J, Feliciano C, Ting JT, Wang W, Wells MF, Venkatraman TN, et al. Shank3 mutant mice display autistic-like behaviours and striatal dysfunction. Nature. 2011;472:437–42.
22. Caruso A, Marconi MA, Scattoni ML, Ricceri L. Ultrasonic vocalizations in laboratory mice: strain, age and sex differences. Genes Brain Behav. 2022;21:e12815.
23. Kalinowska M, van der Lei MB, Kitiashvili M, Mamcarz M, Oliveira MM, Longo F, et al. Deletion of Fmr1 in parvalbumin-expressing neurons results in dysregulated translation and selective behavioral deficits associated with fragile X syndrome. Mol Autism. 2022;13:29.
24. Jang WE, Park JH, Park G, Bang G, Na CH, Kim JY, et al. Cntnap2-dependent molecular networks in autism spectrum disorder revealed through an integrative multi-omics analysis. Mol Psychiatry. 2023;28:810–21.
25. Tripathi MK, Ojha SK, Kartawy M, Khaliulin I, Hamoudi W, Amal H. Mutations associated with autism lead to similar synaptic and behavioral alterations in both sexes of male and female mouse brain. Sci Rep. 2024;14:10.
26. Liang B, Zhang L, Barbera G, Fang W, Zhang J, Chen X, et al. Distinct and Dynamic ON and OFF Neural Ensembles in the Prefrontal Cortex Code Social Exploration. Neuron. 2018;100:700–714.e9.
27. Nicholson C, Freeman JA. Theory of current source-density analysis and determination of conductivity tensor for anuran cerebellum. J Neurophysiol. 1975;38:356–68.
28. Kumar SS, Huguenard JR. Properties of excitatory synaptic connections mediated by the corpus callosum in the developing rat neocortex. J Neurophysiol. 2001;86:2973–85.
29. Douglas RJ, Koch C, Mahowald M, Martin KAC, Suarez HH. Recurrent excitation in neocortical circuits. Science. 1995;269:981–5.
30. Kisvárday ZF, Martin KA, Freund TF, Maglóczky Z, Whitteridge D, Somogyi P. Synaptic targets of HRP-filled layer III pyramidal cells in the cat striate cortex. Exp Brain Res. 1986;64:541–52.
31. Sacai H, Sakoori K, Konno K, Nagahama K, Suzuki H, Watanabe T, et al. Autism spectrum disorder-like behavior caused by reduced excitatory synaptic transmission in pyramidal neurons of mouse prefrontal cortex. Nat Commun. 2020;11:5140.
32. Anastasiades PG, Carter AG. Circuit organization of the rodent medial prefrontal cortex. Trends Neurosci. 2021;44:550–63.
33. Ferguson BR, Gao WJ. Thalamic control of cognition and social behavior via regulation of gamma-aminobutyric acidergic signaling and excitation/inhibition balance in the medial prefrontal cortex. Biol Psychiatry. 2018;83:657–69.
34. Ko J. Neuroanatomical substrates of rodent social behavior: the medial prefrontal cortex and its projection patterns. Front Neural Circuits. 2017;11:41.
35. Testa-Silva G, Loebel A, Giugliano M, de Kock CPJ, Mansvelder HD, Meredith RM. Hyperconnectivity and slow synapses during early development of medial prefrontal cortex in a mouse model for mental retardation and autism. Cereb Cortex. 2012;22:1333–42.
36. Pirone A, Alexander JM, Koenig JB, Cook-Snyder DR, Palnati M, Wickham RJ, et al. Social stimulus causes aberrant activation of the medial prefrontal cortex in a mouse model with autism-like behaviors. Front Synaptic Neurosci. 2018;10:35.
37. Lee AT, Gee SM, Vogt D, Patel T, Rubenstein JL, Sohal VS. Pyramidal neurons in prefrontal cortex receive subtype-specific forms of excitation and inhibition. Neuron. 2014;81:61–8.
38. Ramaswamy S, Markram H. Anatomy and physiology of the thick-tufted layer 5 pyramidal neuron. Front Cell Neurosci. 2015;9:233.
39. Rubenstein JLR, Merzenich MM. Model of autism: increased ratio of excitation/inhibition in key neural systems. Genes Brain Behav. 2003;2:255–67.
40. Wong RKS, Chuang SC, Bianchi R. Metabotropic Glutamate Receptors and Epileptogenesis. Epilepsy Curr. 2002;2:81–5.
41. Peixoto RT, Wang W, Croney DM, Kozorovitskiy Y, Sabatini BL. Early hyperactivity and precocious maturation of corticostriatal circuits in Shank3B−/− mice. Nat Neurosci. 2016;19:716–24.
42. Peixoto RT, Chantranupong L, Hakim R, Levasseur J, Wang W, Merchant T, et al. Abnormal striatal development underlies the early onset of behavioral deficits in shank3B mice. Cell Rep. 2019;29:2016–2027.e4.
43. Luo YF, Lu L, Song HY, Xu H, Zheng ZW, Wu ZY, et al. Divergent projections of the prelimbic cortex mediate autism- and anxiety-like behaviors. Mol Psychiatry. 2023;28:2343–54.
44. Lazaro MT, Taxidis J, Shuman T, Bachmutsky I, Ikrar T, Santos R, et al. Reduced prefrontal synaptic connectivity and disturbed oscillatory population dynamics in the CNTNAP2 Model of Autism. Cell Rep. 2019;27:2567–2578.e6.
45. Kalmbach BE, Johnston D, Brager DH. Cell-Type Specific Channelopathies in the Prefrontal Cortex of the fmr1-/y Mouse Model of Fragile X Syndrome. eNeuro. 2015;2:ENEURO.0114–15.2015.
46. Brill J, Huguenard JR. Sequential changes in AMPA receptor targeting in the developing neocortical excitatory circuit. J Neurosci. 2008;28:13918–28.
47. Kroon T, van Hugte E, van Linge L, Mansvelder HD, Meredith RM. Early postnatal development of pyramidal neurons across layers of the mouse medial prefrontal cortex. Sci Rep. 2019;9:5037.
48. Durand CM, Betancur C, Boeckers TM, Bockmann J, Chaste P, Fauchereau F, et al. Mutations in the gene encoding the synaptic scaffolding protein SHANK3 are associated with autism spectrum disorders. Nat Genet. 2007;39:25–7.
49. Ha HTT, Leal-Ortiz S, Lalwani K, Kiyonaka S, Hamachi I, Mysore SP, et al. Shank and zinc mediate an AMPA receptor subunit switch in developing neurons. Front Mol Neurosci. 2018;11:405.
50. Gogolla N, LeBlanc JJ, Quast KB, Südhof TC, Fagiolini M, Hensch TK. Common circuit defect of excitatory-inhibitory balance in mouse models of autism. J Neurodev Disord. 2009;1:172–81.
51. Antoine MW, Langberg T, Schnepel P, Feldman DE. Increased excitation-inhibition ratio stabilizes synapse and circuit excitability in four autism mouse models. Neuron. 2019;101:648–661.e4.
52. Shih YC, Nelson L, Janeček M, Matarazzo M, D'Agostino A, Peixoto RT. Early postnatal dysfunction of ACC PV interneurons in Shank3B$^{-/-}$ mice. Mol Psychiatry. 2025;30:5283–99.
53. Chen Q, Deister CA, Gao X, Guo B, Lynn-Jones T, Chen N, et al. Dysfunction of cortical GABAergic neurons leads to sensory hyper-reactivity in a Shank3 mouse model of ASD. Nat Neurosci. 2020;23:520–32.
54. Guo B, Liu T, Choi S, Mao H, Wang W, Xi K, et al. Restoring thalamocortical circuit dysfunction by correcting HCN channelopathy in Shank3 mutant mice. CR Med. 2024;5:101534.
55. Marmolejo N, Paez J, Levitt JB, Jones LB. Early postnatal lesion of the medial dorsal nucleus leads to loss of dendrites and spines in adult prefrontal cortex. Dev Neurosci. 2012;34:463–76.
56. Qin L, Ma K, Yan Z. Chemogenetic activation of prefrontal cortex in shank3-deficient mice ameliorates social deficits, NMDAR hypofunction, and Sgk2 downregulation. iScience. 2019;17:24–35.
57. Benoit LJ, Holt ES, Posani L, Fusi S, Harris AZ, Canetta S, et al. Adolescent thalamic inhibition leads to long-lasting impairments in prefrontal cortex function. Nat Neurosci. 2022;25:714–25.
58. Venkatesan S, Binko MA, Mielnik CA, Ramsey AJ, Lambe EK. Deficits in integrative NMDA receptors caused by Grin1 disruption can be rescued in adulthood. Neuropsychopharmacol. 2023;48:1742–51.
59. Fatemi SH, Folsom TD, Reutiman TJ, Thuras PD. Expression of GABAB receptors is altered in brains of subjects with autism. Cerebellum. 2009;8:64–9.
60. Mejias R, Adamczyk A, Anggono V, Niranjan T, Thomas GM, Sharma K, et al. Gain-of-function glutamate receptor interacting protein 1 variants alter GluA2 recycling and surface distribution in patients with autism. Proc Natl Acad Sci USA. 2011;108:4920–5.
61. Mangano GD, Riva A, Fontana A, Salpietro V, Mangano GR, Nobile G, et al. *De novo GRIN2A* variants associated with epilepsy and autism and literature review. Epilepsy Behav. 2022;129:108604.

62. Duffney LJ, Wei J, Cheng J, Liu W, Smith KR, Kittler JT, et al. Shank3 deficiency induces NMDA receptor hypofunction via an actin-dependent mechanism. J Neurosci. 2013;33:15767–78.
63. Contestabile A, Kojovic N, Casarotto G, Delavari F, Hagmann P, Schaer M, et al. Translational research approach to social orienting deficits in autism: the role of superior colliculus-ventral tegmental pathway. Mol Psychiatry. 2025;30:3729–39.
64. Jung S, Park M. Shank postsynaptic scaffolding proteins in autism spectrum disorder: Mouse models and their dysfunctions in behaviors, synapses, and molecules. Pharmacol Res. 2022;182:106340.
65. Selimbeyoglu A, Kim CK, Inoue M, Lee SY, Hong ASO, Kauvar I, et al. Modulation of prefrontal cortex excitation/inhibition balance rescues social behavior in *CNTNAP2* -deficient mice. Sci Transl Med. 2017;9:eaah6733.
66. Harris KD, Shepherd GMG. The neocortical circuit: themes and variations. Nat Neurosci. 2015;18:170–81.
67. Collins DP, Anastasiades PG, Marlin JJ, Carter AG. Reciprocal circuits linking the prefrontal cortex with dorsal and ventral thalamic nuclei. Neuron. 2018;98:366–379.e4.
68. Wang W, Rein B, Zhang F, Tan T, Zhong P, Qin L, et al. Chemogenetic activation of prefrontal cortex rescues synaptic and behavioral deficits in a mouse model of 16p11.2 deletion syndrome. J Neurosci. 2018;38:5939–48.
69. Ultrasonic Vocalizations in Rat and Mouse Pups - Hofer - 2001 - Current Protocols in Neuroscience - Wiley Online Library. Available from: https://currentprotocols.onlinelibrary.wiley.com/doi/abs/10.1002/0471142301.ns0814s17. [cited 2024 Sep 8].
70. Premoli M, Baggi D, Bianchetti M, Gnutti A, Bondaschi M, Mastinu A, et al. Automatic classification of mice vocalizations using machine learning techniques and convolutional neural networks. PLoS One. 2021;16:e0244636.
71. Pennington ZT, Dong Z, Feng Y, Vetere LM, Page-Harley L, Shuman T, et al. ezTrack: An open-source video analysis pipeline for the investigation of animal behavior. Sci Rep. 2019;9:19979.
72. Goto T, Hatanaka R, Ogawa T, Sumiyoshi A, Riera J, Kawashima R. An evaluation of the conductivity profile in the somatosensory barrel cortex of Wistar rats. J Neurophysiol. 2010;104:3388–412.
73. Griffith WH, Brown TH, Johnston D. Voltage-clamp analysis of synaptic inhibition during long-term potentiation in hippocampus. J Neurophysiol. 1986;55:767–75.
74. Arshadi C, Günther U, Eddison M, Harrington KIS, Ferreira TA. SNT: a unifying toolbox for quantification of neuronal anatomy. Nat Methods. 2021;18:374–7.
75. Vantomme G, Rovó Z, Cardis R, Béard E, Katsioudi G, Guadagno A, et al. A thalamic reticular circuit for head direction cell tuning and spatial navigation. Cell Rep. 2020;31:107747.

ACKNOWLEDGEMENTS

We thank all past and current lab members for their valuable feedback throughout this project. We are grateful to Katlin Villar, Cameron Glick, and Nicole Agranonik for their assistance in managing mouse lines, laboratory equipment, and supplies. We also thank Laura Denardo and Rui Peixoto and their team for their invaluable advice on P0 virus injections.

AUTHOR CONTRIBUTIONS

Gabrielle Devienne: Data collection, Conceptualization, Software, Formal analysis, Investigation, Writing - Original Draft, Visualization, Funding acquisition; Gil Vantomme: Data collection, Software, Validation, Formal analysis, Investigation; John R Huguenard: Conceptualization, Software, Writing - Original Draft, Funding acquisition.

FUNDING

This work was supported by SFARI award # 633450, Screening for convergence of axonal dysfunction across diverse mouse models of autism.

COMPETING INTERESTS

The authors declare no competing interests.

ADDITIONAL INFORMATION

Supplementary information The online version contains supplementary material available at https://doi.org/10.1038/s41380-025-03390-6.

Correspondence and requests for materials should be addressed to John R. Huguenard.

Reprints and permission information is available at http://www.nature.com/reprints

Publisher's note Springer Nature remains neutral with regard to jurisdictional claims in published maps and institutional affiliations.

Springer Nature or its licensor (e.g. a society or other partner) holds exclusive rights to this article under a publishing agreement with the author(s) or other rightsholder(s); author self-archiving of the accepted manuscript version of this article is solely governed by the terms of such publishing agreement and applicable law.